LBL-10204 c.2
Preprint

Lawrence Berkeley Laboratory
UNIVERSITY OF CALIFORNIA

Submitted to Physical Review C

DOMINANCE OF STRONG ABSORPTION IN $^{9}Be + ^{28}Si$ ELASTIC SCATTERING

M. S. Zisman, J. G. Cramer, D. A. Goldberg,
J. W. Watson, and R. M. DeVries

December 1979

Prepared for the U.S. Department of Energy under Contract W-7405-ENG-48

DISCLAIMER

DOMINANCE OF STRONG ABSORPTION IN $^{9}Be + ^{28}Si$ ELASTIC SCATTERING

M. S. Zisman
Lawrence Berkeley Laboratory, Berkeley, CA 94720

and

J. G. Cramer
Physics Department, University of Washington, Seattle, WA 98195

and

D. A. Goldberg
Cyclotron Laboratory, University of Maryland, College Park, MD 20742

and

J. W. Watson
Physics Department, Kent State University, Kent, Ohio 44242

and

R. M. DeVries
Los Alamos Scientific Laboratory, Los Alamos, NM 87545

ABSTRACT

The elastic scattering of $^{9}Be + ^{28}Si$ has been measured at laboratory energies of 121.0 and 201.6 MeV. These data have been combined with existing lower energy $^{9}Be + ^{28}Si$ data in order to carry out a global optical model analysis. Calculations employing Woods-Saxon potentials yield good fits to the data without requiring explicitly energy-dependent parameters. In contrast, using a proximity form for the real potential requires an explicitly energy dependent Woods-Saxon imaginary potential in order to achieve comparable quality fits. Notch perturbation calculations have been utilized to locate the radial region of the potential to which the scattering is sensitive. At all energies the imaginary potential is stronger than the real potential at the radius

of maximum sensitivity. This dominance of the absorptive potential greatly limits the amount of information which can be gained about the real potential. Comparison of the $^{9}Be + ^{28}Si$ system with other light heavy ion systems such as $^{6}Li + ^{28}Si$, $^{12}C + ^{28}Si$, and $^{16}O + ^{28}Si$ suggests that the weak binding of ^{9}Be may be responsible for the strong absorption in this case.

[NUCLEAR REACTIONS ^{28}Si (^{9}Be, ^{9}Be), E_L = 121.0 and 201.6 MeV, measured $d\sigma/d\Omega$; optical model analysis; deduced Woods-Saxon and proximity model optical parameters, V/W ratios, fusion barriers. Comparison with ^{6}Li + ^{28}Si and ^{16}O + ^{28}Si behavior.]

I. Introduction

In recent years we have been involved in a systematic study[1,2] of the elastic scattering of various light heavy ion projectiles from ^{28}Si. Our goal is to gain a better understanding of this relatively simple heavy ion interaction process. For example, we wish to learn about the energy dependence of the optical potentials, the sensitivity to the real or imaginary well depths, the "projectile dependence" of the interaction, and whether heavy ions show evidence for nuclear "rainbow" scattering (as is found[3] for light ion projectiles).

The ansatz for this study will be the same as that used in previous work: We combine our high energy measurements with existing lower energy data[4-6] in order to perform global optical model searches. In addition, we begin with a simple assumption about the interaction - that it can be described by a potential having no explicit energy dependence. The neglect of the energy dependence of the real potential (due to non-locality of the nucleon-nucleon force) is expected to be a good approximation for heavy ion projectiles, since the non-locality effects decrease as $1/A_p$.[7] As regards the imaginary potential, the situation is less clear. Our view is that, insofar as it is possible to describe data over a large energy range without explicit energy dependence, the approach is a reasonable one. If the data do not allow such a treatment, then more complicated parametrizations must be sought. We will see below that the question of whether or not the imaginary potential need be explicitly energy dependent depends quite strongly on the choice of the real potential. In particular, using a non-Woods-

Saxon (WS) shape, such as a folded or proximity real potential, seems to require a marked energy dependence in the imaginary potential.

Based on our previous work,[1,2] we have been able to separate the characteristics of the projectiles investigated into two classifications, which we refer to as "light ion" and "heavy ion" behavior. In the case of light ion behavior, e.g., ^{4}He, it is found[3] that: a) nuclear rainbow scattering is observed at high energies; b) the fitted potentials are dominated by the real potential, that is $V/W \sim 5$ (in the central region); and c) the fitted potentials are energy dependent. In contrast, for heavy ions, e.g., ^{16}O, we find[1,2]: a) no evidence for nuclear rainbow scattering; b) the fitted potentials have $V/W \sim 1$ (in the nuclear surface); and c) it <u>is</u> possible to find energy independent potentials which fit data over a very large energy range, provided a shallow real well ($V_o \sim 10$ MeV) is chosen.

In Ref. 2 it was shown that the elastic scattering of $^{12}C + ^{28}Si$ exhibits heavy ion behavior very similar to the $^{16}O + ^{28}Si$ system.[1] In contrast, the $^{6}Li + ^{28}Si$ system[2] behaves in a qualitatively different fashion. In particular, the ^{6}Li data at $E_L = 135.1$ MeV do exhibit the characteristic exponential falloff of nuclear rainbow scattering. As is true for α-particle elastic scattering,[3] a reasonable fit to the high energy data requires a real well depth $V_o \gtrsim 100$ MeV. Furthermore, it has not been possible to fit $^{6}Li + ^{28}Si$ data over a large energy range with an energy independent WS potential. For these reasons we classify the $^{6}Li + ^{28}Si$ system as one which exhibits light ion behavior.

Because the character of the elastic scattering from a ^{28}Si target changes markedly from ^{6}Li to ^{12}C projectiles, we have undertaken a study of the intermediate ^{9}Be + ^{28}Si system in order to map out the transition region. In addition, ^{9}Be shares a number of properties in common with ^{6}Li, namely, both have ground states which are not spin-zero and both are quite weakly bound compared with other projectiles studied. Comparison of the ^{6}Li and ^{9}Be behavior might therefore be expected to shed some light on the question of whether or not the differences between ^{6}Li and ^{12}C elastic scattering are related to these properties of ^{6}Li.

II. Experimental

The elastic scattering of $^{9}Be + ^{28}Si$ has been studied at laboratory energies of 121.0 and 201.6 MeV using ^{9}Be (3+) and ^{9}Be (4+) beams from the LBL 88-Inch Cyclotron. Data were measured with an array of four 2.5 mm thick Si(Li) detectors mounted in a 91 cm diameter scattering chamber. The beam spot size at the target was about 1.5 x 3 mm; the calculated divergence is roughly 0.5°. The individual counters in the array had an angular acceptance of 0.25° and a spacing of 2°; each had a solid angle of 0.13 msr. Measurements were made in 0.5° steps at forward angles and 1° steps at backward angles. The angular range covered was 3° to 22° at 201.6 MeV and 3° to 34° at 121.0 MeV.

Absolute angles were determined by making comparative measurements on both sides of the beam axis. Fluctuations in the beam direction were monitored and corrected for in the analysis by means of a suitably placed monitor detector. The monitor angle was chosen to correspond to a rapidly changing region of the oscillatory forward angle elastic angular distribution. Since the inelastic angular distribution of the $^{28}Si(2^+)$ state at 1.78 MeV excitation is oscillating out of phase with the elastic, the $0^+/2^+$ ratio is an extremely sensitive measure of the scattering angle. Using this ratio easily allows detection of beam angle changes as small as ±0.05°.

The thickness of the self-supporting, enriched ^{28}Si target was 380 $\mu g/cm^2$. It was determined by comparing the elastic cross section to that of a ^{nat}Si target which was later weighed. Relative errors were obtained for each point by adding in quadrature the error due

to angular uncertainty and the statistical error. The former error dominates at the forward angles and is essentially negligible thereafter. Absolute cross sections measured here are estimated to have an uncertainty of ±10%.

The data were stored in an analyzer based on a TI-960A computer and transferred to a ModComp IV/25 computer where they were written on tape for subsequent analysis.

III. Results and Discussion

A. Woods-Saxon Potentials

As mentioned earlier, we begin by looking for a potential which requires no explicit energy dependence. We use a WS shape for both the real and imaginary potentials:

$$V(r) = -V_o \left\{1 + \exp\left[(r - R_R)/a_R\right]\right\}^{-1} \tag{1}$$

$$W(r) = -iW_o \left\{1 + \exp\left[(r - R_I)/a_I\right]\right\}^{-1} \tag{2}$$

where

$$R_R = r_R \left(A_p^{1/3} + A_t^{1/3}\right) \tag{3a}$$

$$R_I = r_I \left(A_p^{1/3} + A_t^{1/3}\right) . \tag{3b}$$

For the Coulomb potential we use the standard form:

$$V_C(r) = \frac{Z_p Z_t e^2}{r}, \quad (r > R_C) \tag{4a}$$

$$= \frac{Z_p Z_t e^2}{2R_C}\left[3 - \frac{r^2}{R_C^2}\right], \quad (r < R_C) \tag{4b}$$

where

$$R_C = r_C \left(A_p^{1/3} + A_t^{1/3}\right) . \tag{4c}$$

Global optical model searches were carried out using the code GENOA.[8] Generally the input data consisted of $^{9}Be + ^{28}Si$ elastic scattering cross sections at 13 MeV[5] along with the 121.0 and 201.6 MeV cross sections measured here. Representative examples of the quality of fits obtained are shown in Fig. 1. Parameters for the optical potentials shown in Fig. 1, along with those for other potentials which lead to comparable quality fits, are listed in Table I.

It is apparent from Table I that a wide range of real well depths are allowed by the data, even with the additional constraint of demanding an energy independent potential. For example, the two potentials shown in Fig. 1, G92 and G95, have very similar imaginary wells and yet differ by an order of magnitude in the real well depth. The close similarity of the predicted angular distributions at all three energies demonstrates clearly that in the absence of additional knowledge it will not be possible to extract information about the real well depth in this system. At first glance this does not seem surprising - "heavy ions" are usually assumed to behave this way. However, our previous results[1,2] with ^{16}O and ^{12}C do not show the same lack of sensitivity to the real well. In order to fit $^{16}O + ^{28}Si$ data over a wide energy range with an energy independent potential, it was found that only a shallow real well (set E18 in Table II) gave acceptable results. The $^{12}C + ^{28}Si$ system led to a similar conclusion (set H12 in Table II).

The sensitivity to the real well in the case of ^{12}C and ^{16}O scattering is related to the predicted existence of nuclear rainbow scattering for deep real potentials having moderate absorption. This is illustrated

in Fig. 2 where predictions for $^{16}O + ^{28}Si$ elastic scattering at 215 MeV are compared for two choices of real well depth, V_o = 10 MeV and V_o = 100 MeV. The latter potential, which fits low energy $^{16}O + ^{28}Si$ elastic data (E_{Lab} = 33 - 81 MeV) as well as does the shallow potential, is totally incompatible with the high energy data. (We note that it is possible, if one relaxes the requirement of energy independence, to rectify this discrepancy.[9]) However, we emphasize that in the $^{9}Be + ^{28}Si$ system there is no need to make the imaginary potential energy dependent in order to achieve reasonable agreement with the data, independent of the depth of the real potential.

There is some problem with most of the potentials listed in Table I in reproducing the trend of the larger angle data ($\theta_{c.m.} \sim 25^{o}$) in the 201.6 MeV angular distribution. This defect is improved, as shown in Fig. 3, by using a potential such as G38. (Although the parameters of potential G38 are somewhat unusual, it will be seen below that this potential is not very different from the other potentials used here in the important radial region around 5-10 fm.)

We found empirically that the fitting procedure we used tended to overemphasize the high energy data sets. Recently there have appeared[6] some high quality $^{9}Be + ^{28}Si$ scattering data at low energies; it is instructive to see whether or not our potentials can reproduce these data. Figure 4 shows predictions from two of our potentials, G92 and G38, compared with the data and one of the "universal" potentials from Balzer et al.[6] (Set B01 in Table I). It can be seen that potential G92 does not do a completely adequate job at the low energies. (This deficiency is already in evidence, albeit not too visibly, in Fig. 1.)

On the other hand, the fits using potential G38 are quite comparable to those using potential B01. In contrast, Fig. 5 shows that the potential derived from the low energy data alone does not extrapolate well to the high energy data sets measured in this work.

One question we hope to answer in this study concerns the existence of nuclear rainbow scattering in the high energy angular distributions. We know[2,3] that high energy light ions, up to ^{6}Li, do show behavior which is dominated by nuclear rainbow scattering, while ^{12}C and ^{16}O projectiles (see Fig. 2) do not.[1,2] The $^{9}Be + ^{28}Si$ potentials listed in Table I have predicted rainbow angles, θ_R, ranging from -81^{o} to -2^{o}. Thus, one would expect to see evidence for rainbow scattering in the data if V_o is greater than about 75 MeV, provided the absorption is not too strong. This is demonstrated in Fig. 6 which shows the behavior of potential G92 as the imaginary strength is reduced toward zero. Although the predicted value of θ_R is -46^{o}, there is nonetheless an increase in cross section of almost 2 orders of magnitude in the region where data exist. We conclude from this that the absorption required to fit the data is suffcient to remove the observable effects of rainbow scattering in the calculated angular distributions. Although the calculation involving potential G38 (Fig. 3) does show some flattening out at back angles, this is not related to rainbow effects. It can be seen in Fig. 7 that for this potential a reduction of the imaginary strength by a factor of 100 (to W = 5 MeV) makes essentially no change in the magnitude of the predicted cross sections, although the phase of the oscillations shifts markedly.

Based on the classifications outlined in Section I, the above results clearly indicate that ^{9}Be behaves as a "heavy ion" projectile.

B. Other Potential Shapes

1. Folding Model

Satchler[10] has performed an extensive analysis of our high energy $^{9}Be + ^{28}Si$ data and also the low energy data of Balzer et al.[6] utilizing a double-folding model for the real part of the optical potential and a WS imaginary potential. As was true for the $^{16}O + ^{28}Si$ system analyzed earlier,[9] the folding model fits are similar in quality to those obtained with a WS real potential. However, for the $^{9}Be + ^{28}Si$ system the folding model results are anomalous in the sense that a substantial renormalization ($N \sim 0.5$) is required. In other words, the predicted strength of the real potential must be reduced a factor of 2 from the folding model estimate in order to fit the data. Although a substantial number of projectile + target combinations have been studied,[11] only ^{9}Be and ^{6}Li (Ref. 12) appear to require such a large reduction in the predicted strength of the folding-model real potential.

In the folding-model analysis of the $^{16}O + ^{28}Si$ data,[9] a global approach was employed. In order to get agreement with the data, however, it was essential to use a WS imaginary potential having an explicit energy dependence of the diffuseness parameter. Satchler also showed that the same sort of parametrization of the imaginary potential allowed a fit to the ^{16}O data with a deep WS real well, something which was not possible with an energy independent imaginary potential. Unfortunately, no global analysis was performed[10] for the $^{9}Be + ^{28}Si$ system so no systematic behavior of the imaginary potential is available.

2. Proximity Potential

In recent years, it has become more common to analyze heavy ion elastic scattering[13] and also fusion data[14,15] by means of the proximity potential formulation. In the proximity model, the real ion-ion potential is given by:[16]

$$V(\zeta) = 4\pi\gamma\, \bar{C} b\, \phi(\zeta) \tag{5}$$

where the dimensionless distance parameter is

$$\zeta = (r - C_t - C_p)/b \quad . \tag{6}$$

In equation (5),

$$\bar{C} = \frac{C_p C_t}{C_p + C_t} \tag{7}$$

with

$$C_x = R_x \left[1 - (b^2/R_x^2)\right] . \tag{8}$$

In this paper we will use for the universal proximity function the analytic approximation given by Blocki et al.[16],

$$\phi(\zeta) = -0.5(\zeta - 2.54)^2 - 0.0852(\zeta - 2.54)^3, \quad \zeta \leqslant 1.2511 \tag{9a}$$

$$\phi(\zeta) = -3.437 \exp(-\zeta/0.75), \quad \zeta \geqslant 1.2511 \tag{9b}$$

Following Vaz and Alexander,[14] we use suggested values[16] for most of the parameters but allow for some deviation from the standard proximity formulae:

$$R_x = 1.28A_x^{1/3} - 0.76 + 0.8\,A_x^{-1/3} + \Delta R \qquad (10)$$

$$b = 1.0 + \Delta b \qquad (11)$$

$$\gamma = 0.9517\left[1 - \left(\frac{N-Z}{A}\right)^2\right] . \qquad (12)$$

In equations (10) and (11), ΔR and Δb give us the ability to modify the potential slightly. For simplicity, the same ΔR value will be used for both target and projectile radii.

Satchler[9] employed a slightly different parametrization of the proximity potential in his study of the $^{16}O + ^{28}Si$ system. He found that it was possible to get fits comparable in quality to those employing a folding-model or WS real potential, again using an energy dependent imaginary diffuseness.

Our results, using proximity potential P01 in Table I to fit the $^{9}Be + ^{28}Si$ data, are shown in Figs 8 and 9. We found, as did Satchler,[9] that it was not possible to obtain agreement with the data if an energy independent imaginary potential is used. However, as can be seen in Figs. 8 and 9, the agreement with the data is quite good when an energy-dependent imaginary diffuseness is employed. Other possibilities for the energy dependence (e.g., an energy-dependent

value of W_o) were not investigated. In the $^{16}O + ^{28}Si$ system,[1] even a quadratic energy dependence of W_o was unsuccessful compared to the approach utilized here.

The optimum values for ΔR and Δb in Eqs. (10) and (11) are 0.059 fm and 0.078 fm, respectively. In the important radial region, these correspond to increasing the real potential by about 25 - 50% compared with the standard proximity potential ($\Delta R = \Delta b = 0$). (Note that this modification is in the opposite sense to that required for the folding-model potential discussed earlier.) In Fig. 10 we compare the best WS real potential, G38, with the folding-model potential (N = 0.5) and the proximity potential P01. It is evident that the data define the value of the real potential, at least to some extent, in the radial region around 6-9 fm.

C. Comparison with Other Projectiles

In order to understand why ^{9}Be behaves differently from the other projectiles, it is instructive to examine the potentials which fit the various systems. Fig. 11 shows the radial form of the WS potentials for ^{6}Li, ^{9}Be, and ^{16}O elastic scattering from ^{28}Si. (The behavior and the best-fit potential for ^{12}C are so similar to ^{16}O that the latter projectile can be considered representative of both ions.) Potential parameters may be found in Table I for ^{9}Be and in Table II for the other projectiles. We see in Fig. 11 that there is evidence for a transition in behavior in going from ^{6}Li to ^{16}O. For ^{6}Li, the imaginary potential exceeds the real potential at large radii (or low energies) while for ^{16}O the real potential is stronger at large radii. The behavior of ^{9}Be is intermediate between these extremes.

In this case the real and imaginary potentials are comparable throughout the tail region, with the imaginary potential somewhat stronger than the real.

The sensitive regions shown in Fig. 11 were obtained from "notch perturbation" calculations.[17] As shown schematically in Fig. 12, this technique involves scanning a radial perturbation across the potential. In radial regions were there is no sensitivity, the χ^2-value of the fit remains unchanged, while in sensitive regions χ^2 worsens dramatically. Figure 13 shows the results of such a scan for the $^{9}Be + ^{28}Si$ system at 201 MeV with potential G38. It can be seen that in this case the sensitive region is about r = 5 - 9 fm and that the radius of maximum sensitivity (for the real potential), R_{sens}, is 6.7 fm. For this particular case the real and imaginary potentials have essentially the same region of sensitivity. In the other cases shown in Fig. 11, the sensitive regions for the real and imaginary potentials are indicated separately. For each projectile, the sensitive region shown in Fig. 11 is evaluated for the highest energy data set available, that is 135.1 MeV ^{6}Li, 201.6 MeV ^{9}Be, and 215.2 MeV ^{16}O.

Although the potentials we have used have no explicit energy dependence, the different real and imaginary well geometries nonetheless give rise to an implicit energy dependence. This is demonstrated for the $^{16}O + ^{28}Si$ system in Fig. 14, where we show the ratio of V/W (evaluated at the radius of maximum sensitivity from the notch perturbation calculations) as a function of energy. We see that for a potential which fits the data, such as E18, the ratio slopes downward as the energy increases,

signifying a gradual increase in the strength of the imaginary compared with the real potential. The behavior of Satcher's "A-type" WS potential[9] is also shown in Fig. 14. This potential has a deep real well but has an imaginary diffuseness which increases with energy; it does about as well as potential E18 in fitting the data. Although not shown in Fig. 14, the proximity model fit to the $^{16}O + ^{28}Si$ data obtained by Satchler[9] behaves very similarly to the "Satchler" curve. Thus, it is clear that the trend shown in Fig. 14 for potential E18 is more or less characteristic of all potentials which fit the $^{16}O + ^{28}Si$ data over the whole energy range. It is worth commenting that the overall trend displayed here for the $^{16}O + ^{28}Si$ system has also been reported for other systems involving this projectile, such as $^{16}O + ^{40}Ca$ (Ref. 18) and ^{16}O + Ni (Ref. 19). For comparison, we also show in Fig. 14 the behavior of potential A23 from Ref. 1. This potential is energy independent and has a deep real well similar to the A-type potential above; it was "adjusted" to fit the high energy by increasing the imaginary strength. (Such an increase has the effect of absorbing away the trajectories which give rise to the large rainbow cross sections generated with the deep real potential. When a shallow real potential such as E18 is used, the rainbow angle moves toward 0^{o} and the effect gets lost in the more familiar Coulomb rainbow region.) Looking at the V/W ratios in Fig. 14, we see that potential A23 behaves very differently than E18 at low energies. We might expect, therefore, that potential A23 will work less well than E18 in this energy range, as is indeed the case.

As shown in Fig. 15, for $^{6}Li + ^{28}Si$ just the opposite trend is observed, with the V/W ratio increasing as the energy increases. In the case of ^{6}Li, it was not possible to find an energy independent potential which fits the high and low energy data sets simultaneously;[2] the curve marked "fits" is obtained from somewhat different potentials at each energy. We have attempted to improve this situation by including various energy dependent parametrizations of both the real and imaginary potential. Thus far it has turned out to be difficult to fit the high and low energy data sets together. This is demonstrated in Fig. 16, where we show WS potential fits to $^{6}Li + ^{28}Si$ data at a number of energies. The solid curve in Fig. 16 is representative of a 6-parameter WS fit to all three energies using potential S01 of Table II. Compared with a potential such as R22 of Ref. 2, this compromise fit causes the χ^2/N value at 135.1 MeV to worsen by a factor of 2; in spite of this the fit at the lowest energy is quite poor. By allowing an explicitly energy-dependent imaginary well depth (potential S02), it is possible to improve the fit to the low energy data set with some additional worsening of the high energy fit. Unfortunately, such improvement corresponds to a substantial worsening of the fit at 46 MeV. We note that for a WS shape, an optimum energy dependent fit leads to a <u>negative</u> energy dependence, that is W decreases with increasing energy. This aspect is consistent with the trend evidenced in Fig. 15 but is very unusual from a phenomenological point of view.[20] This point will be discussed further below.

Recently Tabor et al.[21] attempted to apply the proximity formalism to the scattering of light ions. They found that, while the formalism itself appeared to work, certain discrepancies were apparent. Firstly, the effective projectile radius required by the data was larger than the model prediction[16] (in agreement with the present results) and secondly, the effective ion-ion interaction, $\phi(\zeta)$, was determined to be more steeply rising in both the surface and tail regions than that given by Ref. 16. It is therefore of interest to see how well a proximity potential can do on the ^{6}Li data sets we have studied here. Figure 17 shows results of using proximity potential P10. As with the WS potentials, the fit to the lowest energy data set is quite poor. In contrast to the WS potentials, however, we find that no better agreement with the 135.1 MeV data set is obtained even when it is fitted alone. The combination of a proximity real potential and a WS imaginary potential has difficulty reproducing the smooth back angle rainbow fall-off. This is consistent with the results of Tabor et al.,[21] in essence affirming the inadequate deflecting force represented by the conventional proximity potential of Ref. 16. For the ^{6}Li + ^{28}Si system, the "trick" of using an energy dependent imaginary diffuseness to obtain global fits doesn't help much. As was true with a WS potential (see Fig. 16) improving the 13 MeV fit comes at the expense of the 46 MeV fit. Even the extreme of allowing independently optimized values of a_I at each energy did little to improve things. The resulting values of a_I can be parametrized with a quadratic energy dependence (potential P11). This is basically an exercise in parameter-juggling and is unlikely to have any predictive

power; nonetheless the corresponding fits are shown as the dashed curves in Fig. 17.

The basic problem with fitting the $^{6}Li + ^{28}Si$ data over the whole energy range can be discerned by looking at Fig. 15. The low energy data set requires a very different value of the V/W ratio than do higher energy data sets. In fact the ratio appears to change almost discontinuously at low energies; the high energy data sets are in fair agreement with an energy independent potential. (This statement is confirmed by comparing the potentials discussed here with existing 99 MeV $^{6}Li + ^{28}Si$ data.[22]) Unfortunately, at low energies, the real and imaginary wells are complementary to each other to a large extent. If we compare the potentials which fit the 13 MeV data with those which fit the higher energy data, we find that there are two different types of modification of the high energy potentials which are successful in achieving a fit at 13 MeV. Either the real potential can be decreased by a factor of roughly 3, with the imaginary potential kept the same (e.g., S22 or P12 in Table II), or the imaginary potential can be adjusted to have a steeper fall-off at large radii with the real potential fixed (e.g., S23 or P13). Obviously some combination of these techniques (e.g., R27) also works. In any case, it seems unambiguous that the $^{6}Li + ^{28}Si$ optical potential is very different at 13 MeV than it is at energies above 46 MeV. Possible reasons for this behavior will be discussed below.

Returning now to the $^{9}Be + ^{28}Si$ system, we see in Fig. 18 that the overall trend of V/W is quite flat as a function of energy, with the imaginary potential always being stronger than the real. If we

stretch our faith in a representation of this type, we can infer that for this particular system a 4-parameter WS potential (that is, $r_R = r_I$, $a_R = a_I$) might be adequate over the whole energy range. Figures 19 and 20 show the results of using the 4-parameter potential G05 (see Table I) to fit the data. As expected, the fits are nearly the same quality as those from the 6-parameter potentials. On the other hand, using the folding model potential with a "complex normalization constant" does not yield good fits to the high energy ^{9}Be data,[23] although the optimum V/W ratio, 0.77, is in good agreement with what we find using WS potentials. (The preference for a phenomenological WS shape over a folded shape for the imaginary potential seems to hold for all of the systems studied up to now.[11]) Although there is no theoretical justification for doing so, as an exercise we tried a proximity form for the imaginary as well as the real potential. We found, as for the folding model, that the optimum ratio of V/W was about 0.75, but the fits were rather poor (χ^2/N for the high energy data sets increased by a factor of 5). Thus, for the ^{9}Be + ^{28}Si system, an optical potential having a common geometry for the real and imaginary well is only successful if a WS form is used.

D. Projectile Spin Effects

As mentioned earlier, one difference between the ^{6}Li and ^{9}Be projectiles and the other projectiles we have studied is that both the former have non-zero ground state spins ($J^{\pi} = 1^{+}$ and $3/2^{-}$ for ^{6}Li and ^{9}Be, respectively). In principle, this means that a spin-orbit potential, which we have not considered in our analysis, must contribute to the scattering. One must therefore ask whether ignoring the spin-orbit term leads to incorrect values of the central potential parameters.

Although there is no information on this point for ^{9}Be elastic scattering, the spin-orbit effects in ^{6}Li have been investigated previously both experimentally[24,25] and theoretically.[26] The existence of a spin-orbit term in the interaction potential was demonstrated[24] in a study of ^{6}Li elastic scattering at 20 and 22.8 MeV using a vector polarized ^{6}Li beam on a number of targets, including ^{28}Si. It was shown in this work that the observed asymmetries were consistent with a folding-model estimate[26] of the spin-orbit potential. On the other hand, it was also pointed out that a "reasonable" spin-orbit potential has almost no effect on the predicted angular distributions. Chua et al.[25] made a study of unpolarized ^{6}Li elastic scattering on a variety of targets, but not ^{28}Si, at a higher energy of 50.6 MeV. Their conclusion, based on a standard derivative form for the spin-orbit potential, was that the data gave no unambiguous evidence for spin-orbit effects. Here too the addition of the spin-orbit term had very little observable effect on the angular distributions, the main one being a slight increase in the predicted structure at large angles. (Even this effect could be compensated by slight changes in the imaginary potential.) From these studies[24,25] we conclude that, in terms of angular distributions, the spin-orbit influence is likely to be negligible. Thus, the potentials we extracted from our angular distributions would not be significantly different if a spin-orbit term were explicitly considered. Similar conclusions were reached by Satchler and Love.[12]

Although there are no data from which one can get information on the spin-orbit potential in the case of ^{9}Be elastic scattering, we can use the folding model to estimate the mass dependence of the effect. Amakawa and Kubo[26] have shown that the result of folding the spin-orbit potential over the projectile volume is that the radial form of the spin-orbit term changes from its original derivative form to a volume form, and that the mass dependence is A_p^{-2}. In this case the spin-orbit effects in ^{9}Be elastic scattering would be even smaller than for ^{6}Li and would not be expected to influence our optical model analysis. (Clearly the effect of the spin-orbit potential will increase at high energies and heavier projectile masses due to the larger value of the grazing angular momentum. However, since the centrifugal potential increases much more rapidly with energy than the spin-orbit potential, even at high energies the spin-orbit effects are expected[26] to be small.)

In addition to possible spin-orbit effects, ^{6}Li and ^{9}Be might also be influenced by quadrupole terms in the optical potentials. Satchler and Fulmer[27] have shown that, in a simple coupling model, the (incoherent) contribution from the quadrupole term leads to an additional elastic cross section which is proportional to the cross section for inelastic scattering to the 2^+ state in the core. Because the 2^+ cross section is generally out of phase with the elastic, the practical effect of this term is to damp out the structure in the back angle elastic scattering angular distribution (where σ_{el} and σ_{inel} are more or less comparable in magnitude). Evidence for this sort of behavior has been seen in heavy ion systems similar to the

ones studied here by Parks et al.,[28] who investigated the elastic scattering of ^{10}B and ^{11}B from ^{27}Al at 50 MeV. They find that for $^{10}B + ^{27}Al$ there is substantial damping of the cross sections in the angular region beyond $\theta_{c.m.} = 50^{o}$ compared with a standard optical model prediction. In the case of ^{11}B, the effect is less severe, but some filling-in of the minima is visible. Parks et al. were able to reproduce these trends by adding the quadrupole cross section, calculated with a double-folding model, to the spherical optical model cross section. The importance of the quadrupole term was found[28] to scale roughly as the quadrupole moment of the projectile.

If we try to apply these results to our situation, the following points emerge. Since ^{6}Li has a very small quadrupole moment (-0.8 emb)[29] compared with that for ^{10}B or ^{11}B (80 and 40 emb, respectively),[30] it is unlikely that the quadrupole term is significant in this case. On the other hand, the ^{9}Be quadrupole moment (65 emb)[29] is comparable to those in the boron projectiles. It seems possible, therefore, that the larger angle ^{9}Be data, particularly at 201.6 MeV (Figs. 1,3, and 8), could contain a contribution from this effect. If this is the case, it calls into question to some extent a potential such as G38 (Fig. 3), which more or less reproduces the lack of back angle structure in the high energy ^{9}Be angular distribution. However, the fact that a potential such as G38 is capable of fitting data over such a large energy range argues at the very least that it is possible to successfully incorporate quadrupole effects, if present, into an optical potential. Although calculations such as those reported by Parks et al.[28] are beyond the scope of this paper, they would clearly

be very interesting to perform for the $^{9}Be + ^{28}Si$ system. (It is unfortunate that our experiment does not allow us to observe the ^{9}Be projectile excitation, since the approach of Satchler and Fulmer[27] would then yield a direct estimate of the quadrupole contribution to the elastic scattering.)

E. Breakup

If we look at the trends for the various projectiles indicated in Figs. 14, 15 and 18, we see that ^{16}O behaves in a rather intuitive way, that is, the imaginary potential gets more important as the energy increases. On the other hand, ^{6}Li behaves in the opposite fashion and ^{9}Be shows a stronger imaginary potential at all energies. Because the binding energies of ^{6}Li and ^{9}Be (1.47 and 1.67 MeV, respectively) are very low compared with other light heavy ions, it is tempting, particularly in the case of ^{6}Li, to ascribe the low energy behavior to breakup in the Coulomb field of the target.

The Coulomb breakup mechanism for ^{6}Li has already been demonstrated[31,32] at near-barrier energies on a variety of targets. (Even very near the barrier, however, it has been shown[33] that the nuclear potential plays a role in the breakup process.) In addition, it was shown[32] that the majority of the $^{6}Li \rightarrow \alpha + d$ cross section comes from a sequential mechanism in which ^{6}Li is first inelastically excited to its 2.18 MeV, 3^{+} level. At high energies, on the other hand, there is evidence[34] that the breakup changes to a direct (presumably nuclear) process which does not proceed through the ^{6}Li 2.18 MeV state.

If we assume a Coulomb excitation mechanism is dominant at low energies, it is possible to estimate what effect it might have on the $^{6}Li + ^{28}Si$ optical potential. Love et al.[35] have shown that the main effect shows up in the imaginary potential, which has a long range tail added to it characterized by a strength

$$W_p = 0.01676 \frac{\mu Z_t^2}{k} B(E2) \, g_2 \text{ MeV} \cdot \text{fm}^5, \qquad (13)$$

where μ is the reduced mass (in amu), k is the wave number, g_2 is a tabulated adiabaticity factor and the B(E2), taken from Ref. 36, is in units of $e^2 \cdot fm^4$. Compared with the cases listed in Ref. 35, however, the strength appropriate to $^{6}Li + ^{28}Si$ is more than 2 orders of magnitude weaker; near the sensitive radius at 13 MeV the polarization potential is a few keV, compared with an imaginary strength of about 1 MeV. Thus, it is not clear (sequential) Coulomb breakup is responsible for the low energy behavior.

If one considers instead a breakup process initiated by nuclear inelastic scattering, the conclusion[35] is that the imaginary potential should still be more strongly modified than the real potential. In the nuclear case, no simple expression for the polarization potential is available. Although our experimental technique does not allow us to measure the cross section for projectile excitation of the $^{6}Li(3^+)$ state at 2.18 MeV, it is known from light ion inelastic scattering[37] that this excited state is populated very strongly. In fact, with α particles, the integrated cross section for inelastic scattering is twice that of the elastic. It is in just this situation that channel

coupling may be most important.[38] Assuming the projectile excitation in low energy $^{6}Li + ^{28}Si$ scattering has a similar strength, it seems clear that either a full coupled-channels calculation, or at least an approximate calculation such as proposed by Love et al.[35] should be carried out. It is interesting that, for a fixed real potential, the change required in the imaginary potential at higher energies is that the tail increases (a_I increases). Qualitatively, this is just the sort of behavior which would be expected due to the addition of a polarization potential[35] at the higher energies. The rapid change in the imaginary potential as the energy increases might be related to a change in the strength of the coupling to the elastic channel when the breakup mechanism changes from a sequential to a direct one.[34] Of course depending on the strength of the direct process, in the higher energy regime it may be inappropriate to ignore the explicit channel coupling in obtaining optical potentials. Unfortunately, there is not enough information presently available to answer this question. (As mentioned earlier, the low energy data are equally consistent with a fixed imaginary potential and a markedly weaker real potential. This could conceivably be viewed as symptomatic of the same problem that causes the folding-model real potential to require[12] a substantial reduction for ^{6}Li projectiles. If this were true, one might expect that a "global" folding-model fit to the 13 MeV data would require an even larger renormalization than do the higher energy fits.)

In the ^{9}Be case, Fig. 18 does not indicate any anomaly in the low energy region, although there is some preference here too for the imaginary to increase relative to the real potential at low energies.

There are certain differences in the ^{9}Be breakup compared with ^{6}Li breakup which might explain this fact. Although ^{6}Li breakup at low energies goes mainly through a single state, which is populated predominantly via Coulomb excitation, the ^{9}Be breakup[39] goes through a number of low-lying states. One of these states is reached by an E2 transition with a B(E2) similar[29] to that for the ^{6}Li excited state, but the others are not reached by E2 transitions and are probably excited predominantly by nuclear inelastic scattering. Depending on which states dominate the breakup process at a given energy, it is conceivable that the V/W ratio for ^{9}Be does not change much near the barrier. At higher energies, Stahel et al.[40] have shown that there is a sizable direct breakup cross section in the (^{9}Be, ^{8}Be) reaction at 50 MeV. How, or if, the breakup mechanism changes between the Coulomb barrier and 50 MeV is presently unknown.

F. Fusion

Certain groups[13,18] have recently attempted to fit both elastic and fusion cross sections with a single interaction potential, rather than treating the two types of data independently. Although there is not much information on ^{9}Be + ^{28}Si fusion available, some data have recently been measured[41] which make it worthwhile to compare with predictions from our elastic scattering potentials.

In order to predict fusion cross sections, we must employ a model of the fusion process. Most models[15,42,43] agree that, at low energies, the fusion barrier is determined by the maximum in the real (S-wave potential:

$$V_B = V(R_B) = V_n(R_B) + V_C(R_B) + V_{cent}(\ell, R_B), \qquad (14)$$

where the barrier radius, R_B, is defined by

$$\left.\frac{dV(r)}{dr}\right|_{r = R_B} = 0 \tag{15}$$

In addition, there is a maximum in the fusion cross section at an energy E_{max}, which in some models[13,15] is related to the disappearance of the "pocket" in the real potential for $\ell \geq \ell_{cr}^{max}$ and in other models[43] is related to reaching a critical distance, R_{cr}. The fusion cross section is given by

$$\sigma_f = \pi\lambda\!\!\!^{-2} \sum_{\ell = 0}^{\infty} (2\ell + 1)\, P_\ell \tag{16}$$

where P_ℓ is the fusion probability for partial wave ℓ. In a sharp cut-off (SCO) model,

$$P_\ell = 1 \qquad (\ell \leq \ell_{cr}) \tag{17a}$$

$$= 0 \qquad (\ell > \ell_{cr}) \tag{17b}$$

and ℓ_{cr} is the highest partial wave for which the barrier maximum is below $E_{c.m.}$. Alternatively, the P_ℓ values can be calculated allowing transmission through, as well as passage over, the barrier.[13] Insofar as using a SCO model, i.e., using Eq. (17), predicts essentially the same fusion cross sections except at energies very near the barrier, we have used the simpler approach. The SCO cross sections are then given by:

$$\sigma_f = \pi\lambda\!\!\!^{-2} (\ell_{cr} + 1)^2 \qquad (E \leq E_{max}) \tag{18a}$$

$$= \pi\lambda\!\!\!^{-2} (\ell_{cr}^{max} + 1)^2 \qquad (E > E_{max}) \tag{18b}$$

In the critical radius picture of Glas and Mosel (GM),[43] the fusion probability, P_ℓ, is calculated for transmission through a parabolic barrier. If the approximations of constant barrier curvature and constant barrier radius are made, this model leads to an analytic expression for σ_f in terms of the $\ell = 0$ barrier (see Eqs. (14) and (15)) and the potential at the "critical" radius for fusion:

$$R_{cr} = r_o^{cr} \left(A_p^{1/3} + A_t^{1/3}\right) \tag{19}$$

$$V(R_{cr}) = V_n(R_{cr}) + V_C(R_{cr}), \tag{20}$$

where empirically[43] the value for r_o^{cr} is about 1.0 fm.

Figure 21 shows calculations based on both the SCO and GM models compared with data from Ref. 41. The various parameters needed for the calculations were taken from either potential G38 (solid curves) or the proximity potential (dashed curves) and are listed in Table III. It appears that the data are most consistent with the GM calculation based on potential G38. This is somewhat surprising since in other systems, such as $^{16}O + ^{28}Si$, a GM calculation based on a shallow WS potential such as E18 predicts cross sections much lower than are observed experimentally.[15] A SCO calculation with a deep WS real potential, such as G92, would look fairly similar to the proximity potential calculation shown in Fig. 21. Although a real WS well depth between 13.8 and about 100 MeV is capable of roughly matching the magnitude of the experimental cross sections, the SCO model must produce a downward sloping curve at high energies, in apparent contradiction with the experimental results.[41]

We note that our potentials suggest that the fusion data measured in Ref. 41 are high energy data, in the sense of being beyond the "bend" in the predicted fusion cross sections (see Fig. 21). In the analysis of Ref. 41, the data are assumed to be in the low energy regime of fusion cross sections. This assumption leads[41] to values for the radius and height of the fusion barrier of $R_B = 7.68 \pm 1.02$ fm and $V_B = 22 \pm 4$ MeV. Although the radius extracted from the data is in reasonable agreement with systematics,[14] the barrier height is not and will lead to very different fusion cross sections at near-barrier energies. In spite of there being no low energy data available with which to compare, the values for R_B and V_B obtained from potentials which fit the elastic data (Table III) may be compared with the results of Vaz and Alexander,[14] who made a systematic study of fusion barrier parameters over a very wide range of nuclei. Their parametrization of the barrier parameters is:[14]

$$R_B = r_B \left(A_p^{1/3} + A_t^{1/3}\right) \tag{21a}$$

$$r_B = 2.0337 - 0.2412 \log_{10}(Z_p Z_t) \tag{21b}$$

$$V_B = \frac{Z_p Z_t e^2}{r_e \left(A_p^{1/3} + A_t^{1/3}\right)} \tag{22a}$$

$$r_e = 2.301 - 0.3003 \log_{10}(Z_p Z_t). \tag{22b}$$

For $^{9}Be + ^{28}Si$, this leads to the values $R_B = 8.248$ fm and $V_B = 8.874$ MeV. Agreement with the values obtained in Table III is very good and gives some hope that the potentials we have extracted from the elastic scattering

will be capable of also reproducing low energy fusion cross sections. Clearly the combination of high-quality fusion data along with the available elastic data over a wide energy range will provide an important test of whether or not it is possible to fit both types of data together with a common potential.

One word of caution regarding the GM calculations is clearly in order. It is not implausible that the elastic scattering potential can give information regarding the outer S-wave barrier, but it is much less clear[11] that the optical potential is still "operative" at the smaller separations corresponding to R_{cr}. There is some hope in our case that the optical model V_{cr} is reasonable, however, since the high energy elastic data do have sensitivity into small enough radii to correspond at least roughly to the R_{cr} values.

In the $^{6}Li + ^{28}Si$ system, there is an ambiguity at the lowest energy about whether the required change in the fit potential should be ascribed to the real or the imaginary well. Although hardly a definitive test, it is instructive to compare the predicted fusion barriers of the various real potentials to the Vaz and Alexander systematics.[14] The results, given in Table IV, show that the real potentials obtained from the high energy data lead to fusion barriers consistent with systematics, while the real potentials adjusted to fit the low energy data do not. If we make the assumption that low energy $^{6}Li + ^{28}Si$ fusion data do not show any unusual behavior compared with systematic predictions - a fact not presently verified - we would conclude that

the change in optical potential from low to high energies is most likely related to a change in the tail of the imaginary potential (possibly due to strong coupling to other channels).

IV. Summary

We have measured the elastic scattering of $^{9}Be + ^{28}Si$ at 121.0 and 201.6 MeV and, in combination with other data, have performed a global optical model analysis in the energy range from 12 to 201.6 MeV. In contrast to earlier studies,[1,2] we find that it is possible to obtain a number of energy independent WS potentials, spanning a wide range of real well depths, which fit the data rather well. Optical model calculations employing a proximity form for the real potential have also been performed. Good fits to the data can be obtained provided the parameters of the proximity potential are modified somewhat from their suggested values. In this case it is necessary to employ a WS imaginary potential having an explicit energy dependence in order to reproduce the data. At the highest energy, an examination of the various potentials indicates that there are no visible effects due to nuclear rainbow scattering. However, the data at 201.6 MeV are suggestive of the influence of quadrupole terms in the interaction potential. A calculation of this effect would be very informative to see if this is the case.

Notch perturbation calculations have been performed for the $^{9}Be + ^{28}Si$ potentials obtained here as well as the $^{6}Li + ^{28}Si$ and $^{16}O + ^{28}Si$ potentials studied earlier.[1,2] The sensitive region in ^{9}Be elastic scattering extends from about 5-10 fm, and shows that the imaginary potential is stronger than the real potential throughout. In the case of ^{6}Li elastic scattering, the data indicate that the imaginary potential exceeds the real potential at low energies with the real

potential becoming increasingly important at higher energies, while for ^{16}O the reverse is true. For all systems at all energies we have shown that the ratio of V/W evaluated at the radius of maximum sensitivity is nearly the same for all potentials which fit the data. However, this ratio is not sufficient by itself to map out the potential, probably because the V/W ratio samples the potential at only one point while the scattering itself is sensitive to a fairly large region at any given energy.

Possible explanations of why the low energy ^{6}Li data, and to some extent the ^{9}Be data, are dominated by strong absorption have been considered. One possibility is related to either Coulomb or nuclear breakup at low energies. However, simple estimates of this effect indicate that the expected Coulomb excitation contribution is too small to have a major influence on the $^{6}Li + ^{28}Si$ elastic scattering. It may be that the strength of the coupling to the direct breakup channel is sufficiently large that a full coupled-channels approach will be required; this aspect should be investigated by calculations.

Using two simple models of the fusion process, we have compared our potentials to existing fusion reaction cross sections. The S-wave barrier radius and height extracted from the various potentials agree very well with predictions from fusion systematics. It will be interesting to see how these barrier parameters compare with low energy ^{9}Be fusion data.

V. Acknowledgments

We would like to thank D. L. Hendrie and D. K. Scott for their support of this project and R. A. Gough and the crew of the LBL 88-Inch Cyclotron for providing the ^{9}Be beams used in the experiment. We also thank the authors of Ref. 5 for allowing us to utilize their unpublished data, G. R. Satchler for providing information on his folding-model calculations, and J. Alexander for several informative discussions.

This work was supported in part by the National Science Foundation and in part by the Division of Nuclear Physics, U.S. Department of Energy.

REFERENCES

1. J. G. Cramer, R. M. DeVries, D. A. Goldberg, M. S. Zisman, and C. F. Maguire, Phys. Rev. C 14, 2158 (1976).
2. R. M. DeVries, D. A. Goldberg, J. W. Watson, M. S. Zisman, and J. G. Cramer, Phys. Rev. Lett. 39, 450 (1977).
3. D. A. Goldberg and S. M. Smith, Phys. Rev. Lett. 29, 500 (1975); D. A. Goldberg, S. M. Smith, and G. F. Burdzik, Phys. Rev. C 10, 1367 (1974).
4. J. S. Eck, T. J. Gray, and R. K. Gardner, Phys. Rev. C 16, 1873 (1977).
5. R. M. DeVries, D. S. Shapira, N. Anantaraman, R. Cherry, M. R. Clover, and H. E. Gove, unpublished data.
6. R. Balzer, M. Hugi, B. Kamys, J. Lang, R. Müller, E. Ungricht, and J. Unternährer, Nucl. Phys. A293, 518 (1977).
7. D. F. Jackson and R. C. Johnson, Phys. Lett. 49B, 249 (1974).
8. F. Perey, unpublished.
9. G. R. Satchler, Nucl. Phys. A279, 493 (1977).
10. G. R. Satchler, Phys. Lett. B, to be published.
11. G. R. Satchler and W. G. Love, submitted to Phys. Reports.
12. G. R. Satchler and W. G. Love, Phys. Lett. 76B, 23 (1978).
13. L. C. Vaz, J. M. Alexander, and E. H. Auerbach, Phys. Rev. C 18, 820 (1978); L. C. Vaz and J. M. Alexander, Phys. Rev. C 18, 833 (1978).
14. L. C. Vaz and J. M. Alexander, Phys. Rev. C 18, 2152 (1978).

15. J. R. Birkelund and J. R. Huizenga, Phys. Rev. C 17, 126 (1978); J. R. Birkelund, L. E. Tubbs, J. R. Huizenga, J. N. De and D. Sperber, Phys. Reports 56, 107 (1979).

16. J. Blocki, J. Randrup, W. Swiatecki and C. F. Tsang, Ann. Phys. (N.Y.) 105, 427 (1977).

17. J. G. Cramer, University of Washington Nuclear Physics Laboratory Annual Report 1976, p. 115 (unpublished); J. G. Cramer and R. M. DeVries, Phys. Rev. C, to be published.

18. S. E. Vigdor, D. G. Kovar, P. Sperr, J. Mahoney, A. Menchaca-Rocha, C. Olmer, and M. S. Zisman, submitted to Phys. Rev. C.

19. G. R. Satchler, Phys. Lett. 58B, 408 (1975).

20. H. T. Fortune, A. Richter, R. H. Siemssen, and J. L. Yntema, Phys. Rev. C 20, 648 (1979); R. Vandenbosch, M. P. Webb, and M. S. Zisman, Phys. Rev. Lett. 33, 842 (1974); J. V. Maher, M. W. Sachs, R. H. Siemssen, A. Weidinger, and D. A. Bromley, Phys. Rev. 188, 1665 (1969).

21. S. L. Tabor, D. A. Goldberg, and J. R. Huizenga, Phys. Rev. Lett. 41, 1285 (1978).

22. P. Schwandt, unpublished data.

23. G. R. Satchler, private communication.

24. W. Weiss, P. Egelhof, K. D. Hildenbrand, D. Kassen, M. Makowska-Rzeszutko, D. Fick, H. Ebinghaus, E. Steffens, A. Amakawa, and K. I. Kubo, Phys. Lett. 61B, 237 (1976).

25. L. T. Chua, F. D. Becchetti, J. Jänecke, and F. L. Milder, Nucl. Phys. A273, 243 (1976).

26. H. Amakawa and K. I. Kubo, Nucl. Phys. A266, 521 (1976).

27. G. R. Satchler and C. B. Fulmer, Phys. Lett. 50B, 309 (1974).

28. L. A. Parks, K. W. Kemper, A. H. Lumpkin, R. I. Cutler, L. H. Harwood, D. Stanley, P. Nagel, and F. Petrovich, Phys. Lett. 70B, 27 (1977).

29. F. Ajzenberg-Selove and T. Lauritsen, Nucl. Phys. A227, 1 (1974).

30. G. H. Fuller and V. W. Cohen, Nucl. Data Tables A5, 433 (1969).

31. K. O. Pfeiffer, E. Speth, and K. Bethge, Nucl. Phys. A206, 545 (1973).

32. D. Scholz, H. Gemmeke, L. Lassen, R. Ost, and K. Bethge, Nucl. Phys. A288, 351 (1977).

33. H. W. Wittern, Phys. Lett. 32B, 441 (1970).

34. R. W. Ollerhead, C. Chasman, and D. A. Bromley, Phys. Rev. 134, B74 (1964).

35. W. G. Love, T. Terasawa, and G. R. Satchler, Nucl. Phys. A291, 183 (1977).

36. D. L. Disdier, G. C. Ball, O. Häusser, and R. E. Warner, Phys. Rev. Lett. 27, 1391 (1971).

37. S. Matsuki, S. Yamashita, K. Fukunaga, D. C. Nguyen, N. Fujiwara, and T. Yanabu, J. Phys. Soc. (Japan) 26, 1344 (1969).

38. W. Henning, J. P. Schiffer, D. G. Kovar, S. Vigdor, B. Zeidman, Y. Eisen, and H. J. Körner, Phys. Lett. 58B, 129 (1975).

39. H. Werle, L. Van der Zwan, and K. W. Geiger, Z. Physik 259, 275 (1973).

40. D. P. Stahel, G. J. Wozniak, M. S. Zisman, B. D. Jeltema, and J. Cerny, Phys. Rev. C 16, 1456 (1977).

41. J. S. Eck, J. R. Leigh, T. R. Ophel and P. D. Clark, submitted to Phys. Rev. Lett.

42. R. Bass, Nucl. Phys. A231, 45 (1974).

43. D. Glas and U. Mosel, Nucl. Phys. A237, 429 (1975).

Table I. $^{9}Be + ^{28}Si$ Optical Potentials.[a]

Set	V_o (MeV)	r_R[b] (fm)	a_R (fm)	W_o (MeV)	r_I[b] (fm)	a_I (fm)	θ_R[c] (deg)
G90	300.0	0.567	0.942	41.1	1.054	0.782	-81
G92	150.0	0.703	0.944	27.6	1.150	0.753	-46
G89	100.0	0.767	0.960	23.1	1.191	0.736	-31
G84	75.0	0.776	1.012	29.8	1.143	0.744	-22
G95	15.0	1.149	0.914	24.4	1.185	0.701	-2
G38	13.8	1.244	0.652	503.2	0.617	0.825	-3
G05[d]	13.8	1.232	0.729	16.9	1.232	0.729	-3
B01[e]	10.0	1.162	0.820	20.4	1.162	0.820	0
P01[f]	-	0.059[g]	0.078[h]	17.8	1.241	0.7145[i] (1.20×10^{-3})	-17

a) WS form, except as noted. The Coulomb radius, Eq. (4), is r_C = 1.0 fm unless noted otherwise.

b) See Eq. (3).

c) Value of calculated rainbow angle for the real potential at E_L = 201.6 MeV.

d) Four parameter fit with $r_I = r_R$ and $a_I = a_R$.

e) Taken from Ref. 6, r_C = 0.71 fm.

f) Proximity real potential, see Eqs. (5) - (12) in Sec. III-B(2).

g) Value of ΔR in Eq. (10).

h) Value of Δb in Eq. (11).

i) Energy dependent imaginary diffuseness, $a = a_0 + (a_1) E_L$. The value of a_1 is shown in parentheses.

Table II. ^{6}Li, ^{12}C, and $^{16}O + ^{28}Si$ Optical Potentials.[a]

Ion	Set	V_o (MeV)	r_R[b] (fm)	a_R (fm)	W_o (MeV)	r_I[b] (fm)	a_I (fm)
^{6}Li	R22	150.0	0.727	0.877	44.4	0.904	1.060
	R27	150.0	0.682	0.828	38.8	1.020	0.889
	S01	150.0	0.725	0.874	34.2	1.019	0.904
	S02	150.0	0.725	0.874	51.6[c] (-0.18)	1.112	0.742
	S22	150.0	0.577	0.770	44.4	0.904	1.060
	S23	150.0	0.727	0.877	50.8	1.113	0.743
	P10[d]	-	0.107[e]	0.048[f]	45.5	0.906	1.029
	P11[d]	-	0.107[e]	0.048[f]	45.5	0.906	0.7620[g] (6.3x10^{-3}) [-3.2x10^{-5}]
	P12[d]	-	-0.045[e]	-0.081[f]	45.5	0.906	1.029
	P13[d]	-	0.107[e]	0.048[f]	36.9	1.088	0.770
	Z8	10.0	1.340	0.809	82.1	0.955	0.727
^{12}C	H12	10.0	1.320	0.617	30.3	1.160	0.609
^{16}O	E18	10.0	1.350	0.618	23.4	1.230	0.552
	A23	100.0	0.932	0.797	165.0	0.890	0.764
	S75	100.0	1.060	0.640	42.0	1.060	0.640
	A-type[h]	100.0	0.967	0.745	44.1	1.073	0.605[g] (1.14x10^{-3})

a) WS form, except as noted. The Coulomb radius, Eq. (4), is r_C = 1.0 fm unless noted otherwise. Potentials E18, A23, and S75 are from Ref. 1 and potentials R22, R27, Z8, and H12 are from Ref. 2.

b) See Eq. (3).

c) $W_o = W_1 + (W_2)\, E_L$. The value of W_2 is shown in parentheses.

d) Proximity real potential, see Eqs. (5) - (12) in Sec. III-B(2).

e) Value of ΔR in Eq. (10).

f) Value of Δb in Eq. (11).

g) Energy dependent imaginary diffuseness, $a = a_0 + (a_1)\, E_L + [\, a_2]\, E_L^2$.

h) From Ref. 9, with $r_C = 1.3$ fm.

Table III. Predicted $^{9}Be + ^{28}Si$ Fusion Barriers.

Set	R_B (fm)	V_B (MeV)	R_{cr} [a] (fm)	$V(R_{cr})$ [a] (MeV)
G38	8.145	9.056	5.63	3.90
G05	8.215	8.881	5.63	4.44
G92	8.193	8.699	5.63	-1.30
P01	8.242	8.894	5.63	-4.25
B01 [b]	7.444	9.447	5.63	8.37
Folded [c]	8.066	9.080	5.63	-2.67
Syst. [d]	8.248	8.874	--	--

a) Values of critical radius and critical potential, Eqs. (19) and (20), required for Glas-Mosel calculations. A barrier curvature $\hbar\omega$ = 5 MeV was also used.

b) From Ref. 6. This potential does not reproduce the high energy data sets measured in this work.

c) From Ref. 10, using method B and N = 0.5.

d) From Eqs. (21) and (22), based on Ref. 14.

Table IV. Predicted $^{6}Li + ^{28}Si$ Fusion Barriers.

Set	R_B (fm)	V_B (MeV)
R22[a]	8.099	6.654
S01[a]	8.071	6.677
P10[a]	8.065	6.802
R27[b]	7.558	7.120
P12[b]	7.242	7.485
Syst.[c]	7.971	6.871

a) Preferred for high energy data sets.

b) Preferred for 13 MeV data set.

c) From Eqs. (21) and (22), based on Ref. 14.

FIGURE CAPTIONS

Fig. 1. $^{9}Be + ^{28}Si$ elastic scattering angular distributions at E_L = 13, 121.0, and 201.6 MeV. The curves are representative optical model fits using two of the WS potentials listed in Table I. Values of χ^2/N for potential G95 (G92) are: 13 MeV, 1.4 (2.5); 121.0 MeV, 2.6 (5.1); 201.6 MeV, 2.7 (2.8).

Fig. 2. $^{16}O + ^{28}Si$ elastic scattering angular distribution at E_L = 215.2 MeV (taken from Ref. 1). The solid curve is a fit with a shallow WS potential, E18, and the dashed curve is a prediction using the deeper potential S75 of Table II. Although the deep potential predicts a substantial enhancement of the back angle cross sections due to the existence of nuclear rainbow scattering, the data show no such effect.

Fig. 3. $^{9}Be + ^{28}Si$ elastic scattering angular distributions at E_L = 13, 121.0, and 201.6 MeV. The solid curve is a fit to all three energies using potential G38. Values of χ^2/N for potential G38 are: 13 MeV, 1.2; 121.0 MeV, 10.2; 201.6 MeV, 1.8.

Fig. 4. $^{9}Be + ^{28}Si$ elastic scattering angular distributions at E_L = 12, 20, and 26 MeV. Data are from Ref. 6. Predicted angular distributions are shown for potentials G38 and G92 from this work, along with one of the "universal" potentials from Ref. 6, B01. Values of χ^2/N for potential G38 (G92) [B01] are: 12 MeV, 0.6 (5.0) [0.2]; 20 MeV, 2.0 (25.6) [2.7]; 26 MeV, 1.9 (12.7) [1.5].

Fig. 5. Comparison between predicted and experimental angular distributions for $^{9}Be + ^{28}Si$ elastic scattering at 121.0 and 201.6 MeV. The universal potential B01 from Ref. 6 does not do a good job of reproducing the high energy data.

Fig. 6. Predicted angular distributions for $^{9}Be + ^{28}Si$ elastic scattering at E_L = 201.6 MeV, using the deep potential G92 with various imaginary well depths. As the imaginary strength decreases, a large enhancement in the back angle cross sections due to nuclear rainbow scattering becomes clearly visible.

Fig. 7. Predicted angular distributions for $^{9}Be + ^{28}Si$ elastic scattering, using the shallow potential G38 with two different imaginary well depths. In this case no evidence for a cross section enhancement due to nuclear rainbow scattering is seen because the rainbow effects are so far forward in angle they are dominated by the huge Coulomb rainbow.

Fig. 8. Fits to high energy $^{9}Be + ^{28}Si$ data using the proximity model (potential P01 in Table I). The fits are similar in quality to the WS potential fits shown in Figs. 1 and 3. Values of χ^2/N for potential P01 are: 121.0 MeV, 4.9; 201.6 MeV, 3.1.

Fig. 9. Fits to low energy $^{9}Be + ^{28}Si$ data using the proximity model (potential P01 in Table I). The fits are similar in quality to the WS potential fits shown in Fig. 4. Values of χ^2/N for potential P01 are: 12 MeV, 0.5; 20 MeV, 4.9; 26 MeV, 0.9.

Fig. 10. Comparison of WS (G38), proximity (P01) and folding model (Ref. 10, Method B, N = 0.5) real potentials which fit ^{9}Be + ^{28}Si elastic scattering. The data appear to define the potential reasonably well in the radial region around 6-9 fm.

Fig. 11. Radial form of WS potentials which fit the ^{16}O, ^{9}Be, and ^{6}Li + ^{28}Si systems. ^{9}Be potentials are listed in Table I; those for the other projectiles are listed in Table II. The "sensitive region" for each potential is obtained from a notch perturbation calculation and is shown separately for the real (solid lines) and imaginary (dashed lines) well unless the two regions coincide.

Fig. 12. Example of a WS potential which has been modified by addition of a localized radial perturbation. Varying the position of the perturbation, R_p, produces a sensitivity function such as that shown in Fig. 13.

Fig. 13. Sensitivity function for a radial perturbation such as that in Fig. 12. The "baseline" corresponds to the unperturbed χ^2 value. Radii of the real and imaginary wells along with the turning point of the grazing partial wave ($T_\ell = 0.5$) are indicated for comparison. In this case, the scattering is sensitive to a region from about 5-9 fm, and the "radius of maximum sensitivity," R_s, is about 6.7 fm. In general, R_s decreases as the energy increases and tends to be inside of the strong absorption radius ($D_{1/2}$) used by Satchler (Refs. 9-12).

Fig. 14. Ratio of real to imaginary strength for various $^{16}O + ^{28}Si$ potentials. The curve marked "Satchler" refers to the A-type WS potential from Ref. 9 (see Table II). At each energy the ratio is evaluated at R_s, the radius of maximum sensitivity (for the real potential) from a notch perturbation calculation. For this system, the real potential is stronger at low energies and the imaginary potential becomes more important as the energy increases.

Fig. 15. Same as Fig. 14, but for $^{6}Li + ^{28}Si$. The curve marked "fits" refers to somewhat different potentials at each energy (see text). Potential parameters are given in Table II. For this system, the imaginary potential is stronger at low energies and the real potential becomes more important as the energy increases.

Fig. 16. Fits to $^{6}Li + ^{28}Si$ elastic scattering at 13 MeV (data from J. E. Poling, E. Norbeck, and R. R. Carlson, Phys. Rev. C 13, 648 (1976)), 46 MeV (Ref. 5), and 135.1 MeV (Ref. 2) using an energy independent WS potential (S01) and an energy dependent WS potential (S02). The difficulty in fitting ^{6}Li data over a wide energy range is apparent (see text). Potential parameters are listed in Table II. Values of χ^2 for potential S01 (S02) are: 13 MeV, 21.1 (1.7); 46 MeV, 16.0 (119.5); 135.1 MeV, 5.4 (10.3). Note the different angle scales for the high and low energy data.

Fig. 17. Fits to $^{6}Li + ^{28}Si$ elastic scattering using the proximity model. Parameters are listed in Table II. In contrast to the results of Ref. 2 or Ref. 12, which employed WS and folded potentials, respectively, the combination of a proximity real potential and a WS imaginary potential does not properly reproduce the smooth fall-off of the data in the rainbow region. Values of χ^2/N for potential P10 (P11) are: 13 MeV, 18.0 (9.0); 46 MeV, 14.9 (10.9); 135.1 MeV, 6.1 (6.1). Note the different angle scales for the high and low energy data.

Fig. 18. Same as Fig. 14, but for $^{9}Be + ^{28}Si$. For this system the imaginary potential is stronger than the real potential at all energies.

Fig. 19. Fits to the high energy $^{9}Be + ^{28}Si$ data using a 4-parameter WS potential, G05 (see Table I). Values of χ^2/N for potential G05 are: 121.0 MeV, 4.1; 201.6 MeV, 3.5.

Fig. 20. Fits to the low energy $^{9}Be + ^{28}Si$ data using a 4-parameter WS potential, G05 (see Table I). Values of χ^2/N for potential G05 are: 12 MeV, 0.6; 20 MeV, 4.6; 26 MeV, 1.9.

Fig. 21. Predicted complete fusion cross sections for $^{9}Be + ^{28}Si$, based on parameters extracted from potentials which fit the elastic scattering. The solid lines correspond to potential G38 and the dashed lines to proximity potential P01. Both sharp cut-off (SCO) and Glas-Mosel (GM) calculations (see Sec. III-F) are shown for each potential. (Predictions using a deep WS potential such as G92 would look similar

to the dashed lines.) Data points are from Ref. 41 and the relevant barrier parameters are summarized in Table III. Note the increased cross sections predicted in the GM model compared with the SCO model at low energies due to the consideration of barrier penetrability in the former case.

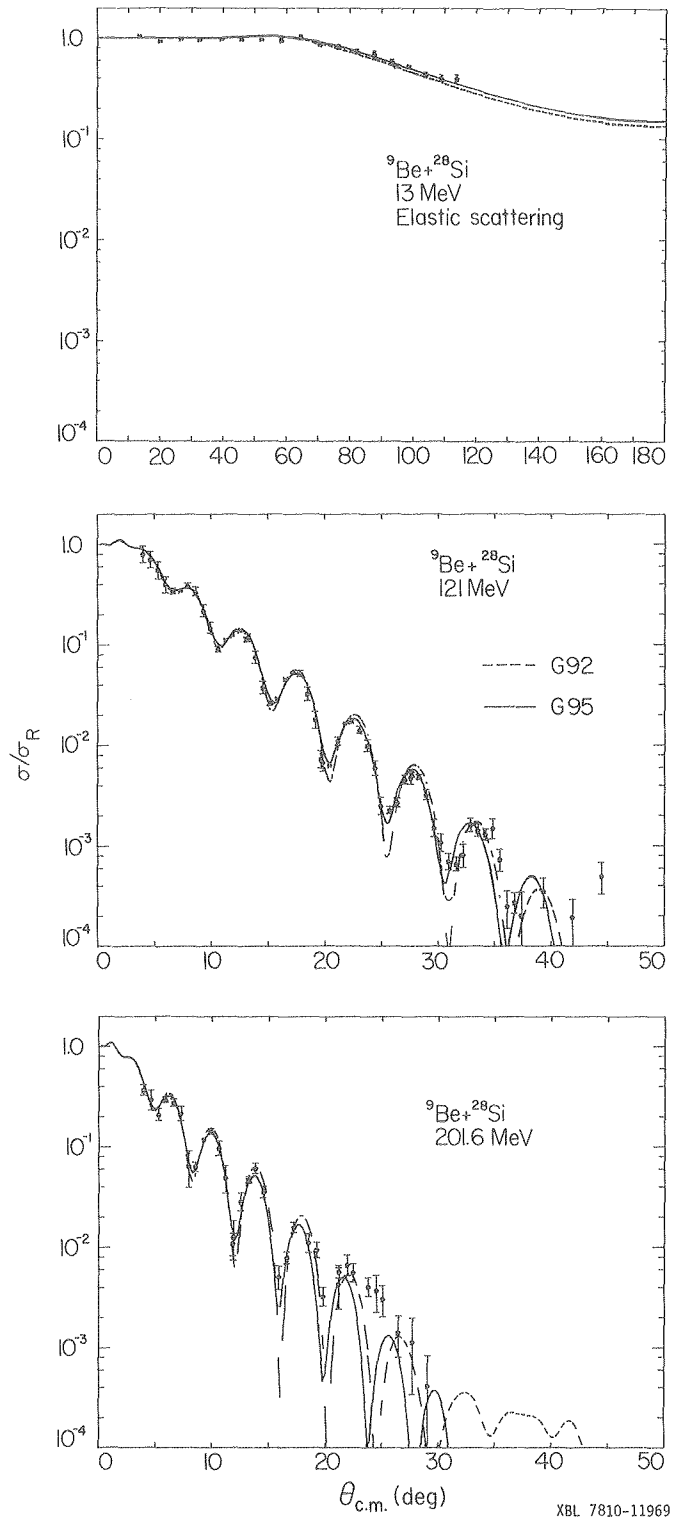
^{9}Be+^{28}Si
13 MeV
Elastic scattering
^{9}Be+^{28}Si
121 MeV
G92
G95
σ/σ_R
^{9}Be+^{28}Si
201.6 MeV
$\theta_{c.m.}$ (deg)
XBL 7810-11969

Fig. 1.

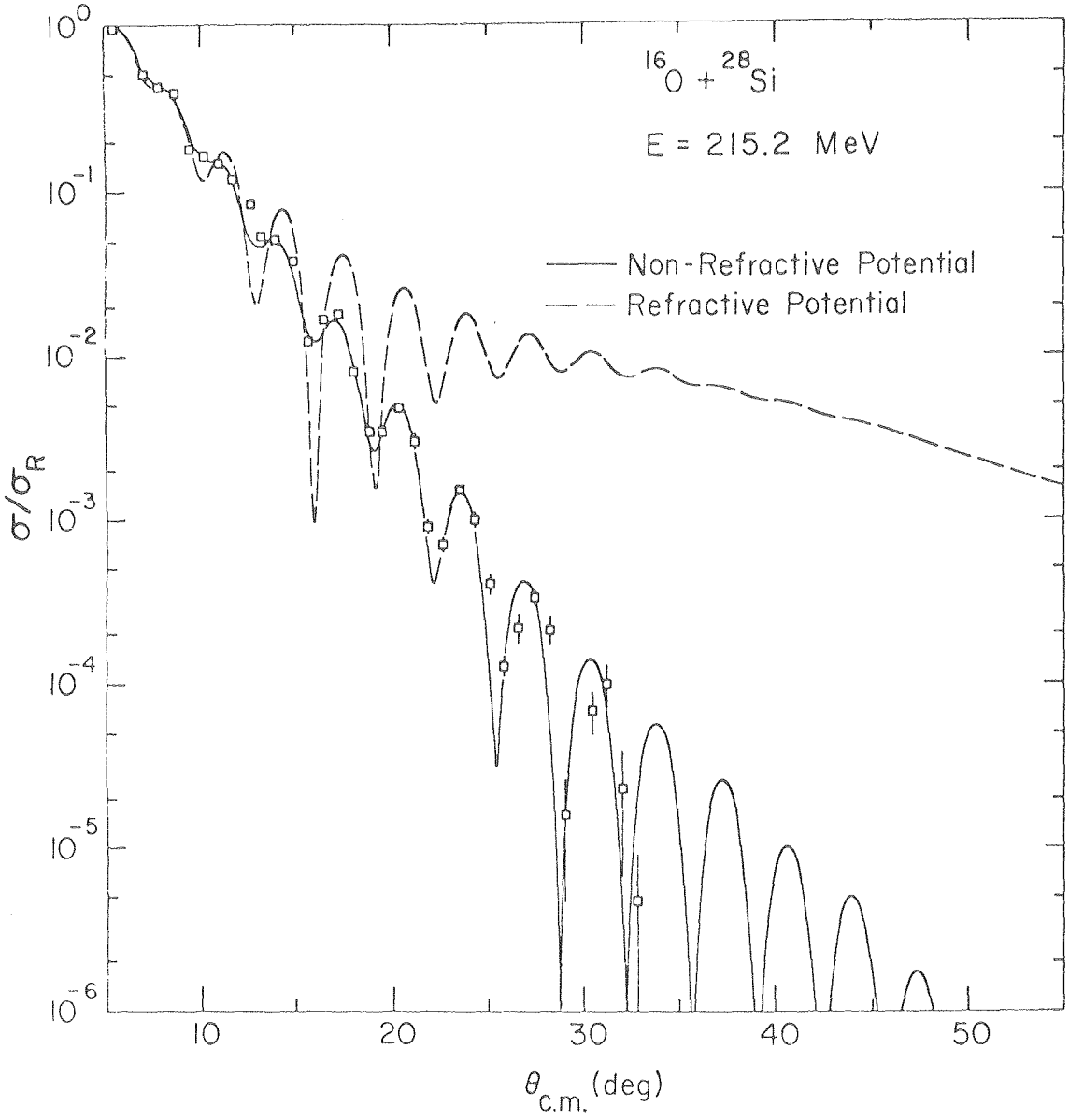

XBL 785-8914

Fig. 2.

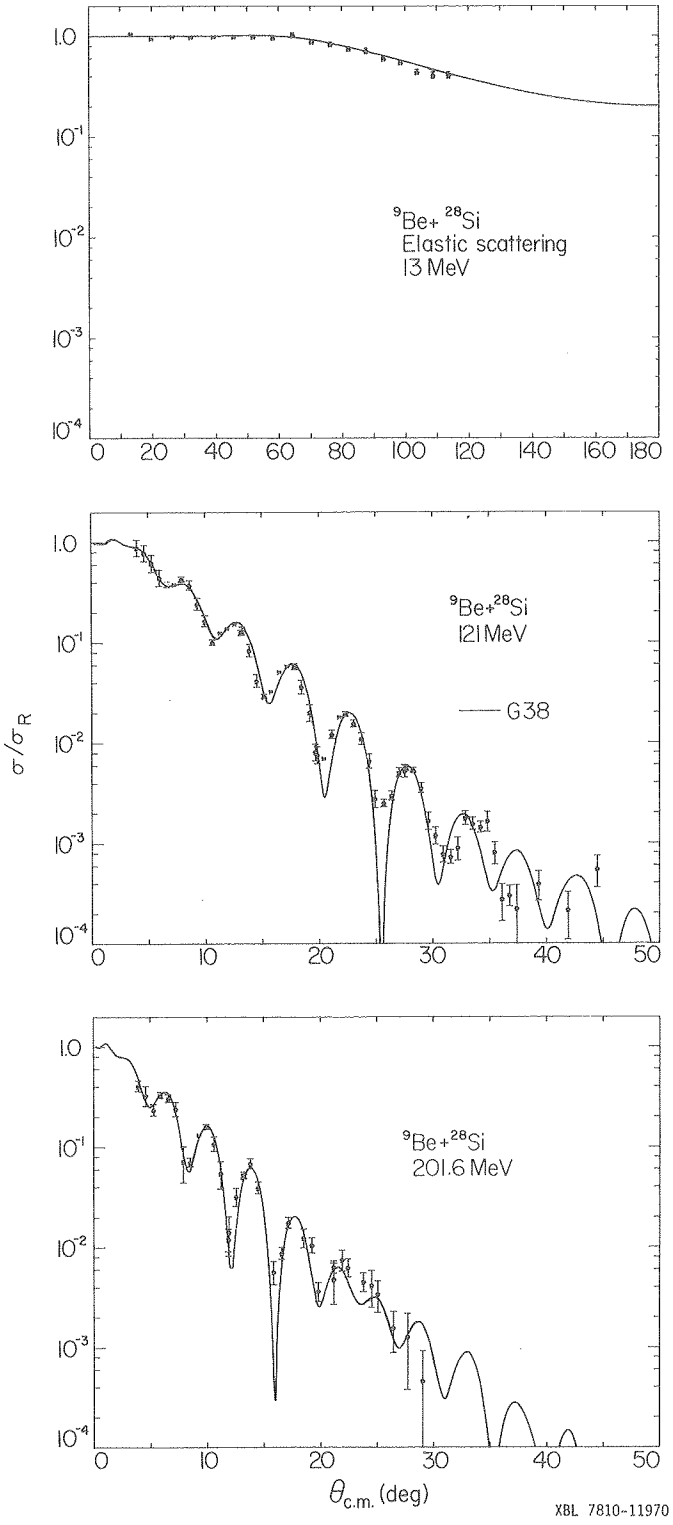
^{9}Be+ ^{28}Si
Elastic scattering
13 MeV
^{9}Be+^{28}Si
121 MeV
G38
^{9}Be+^{28}Si
201.6 MeV
σ/σ_R
$\theta_{c.m.}$ (deg)
XBL 7810-11970

Fig. 3.

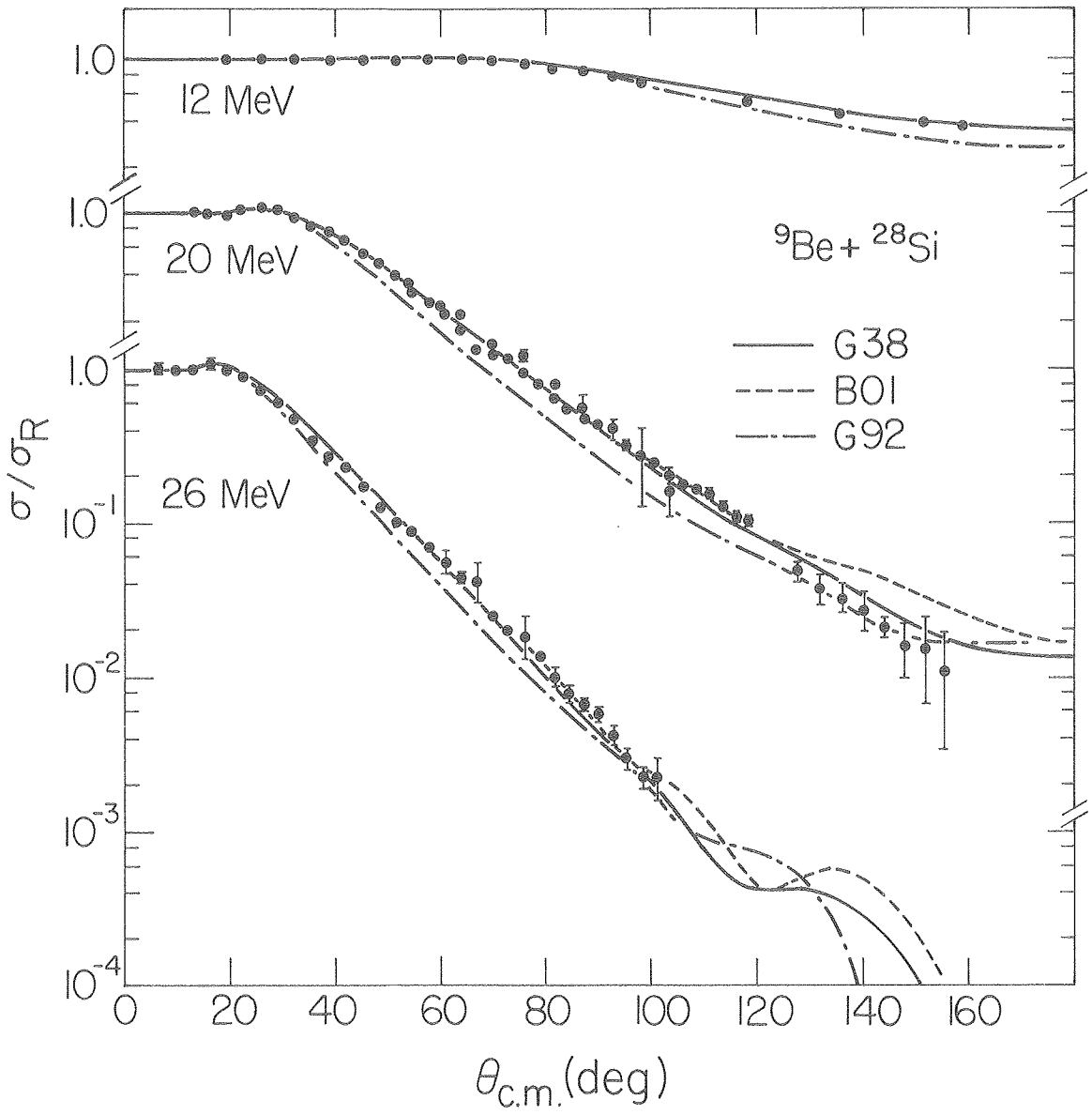

XBL 7911-4532

Fig. 4.

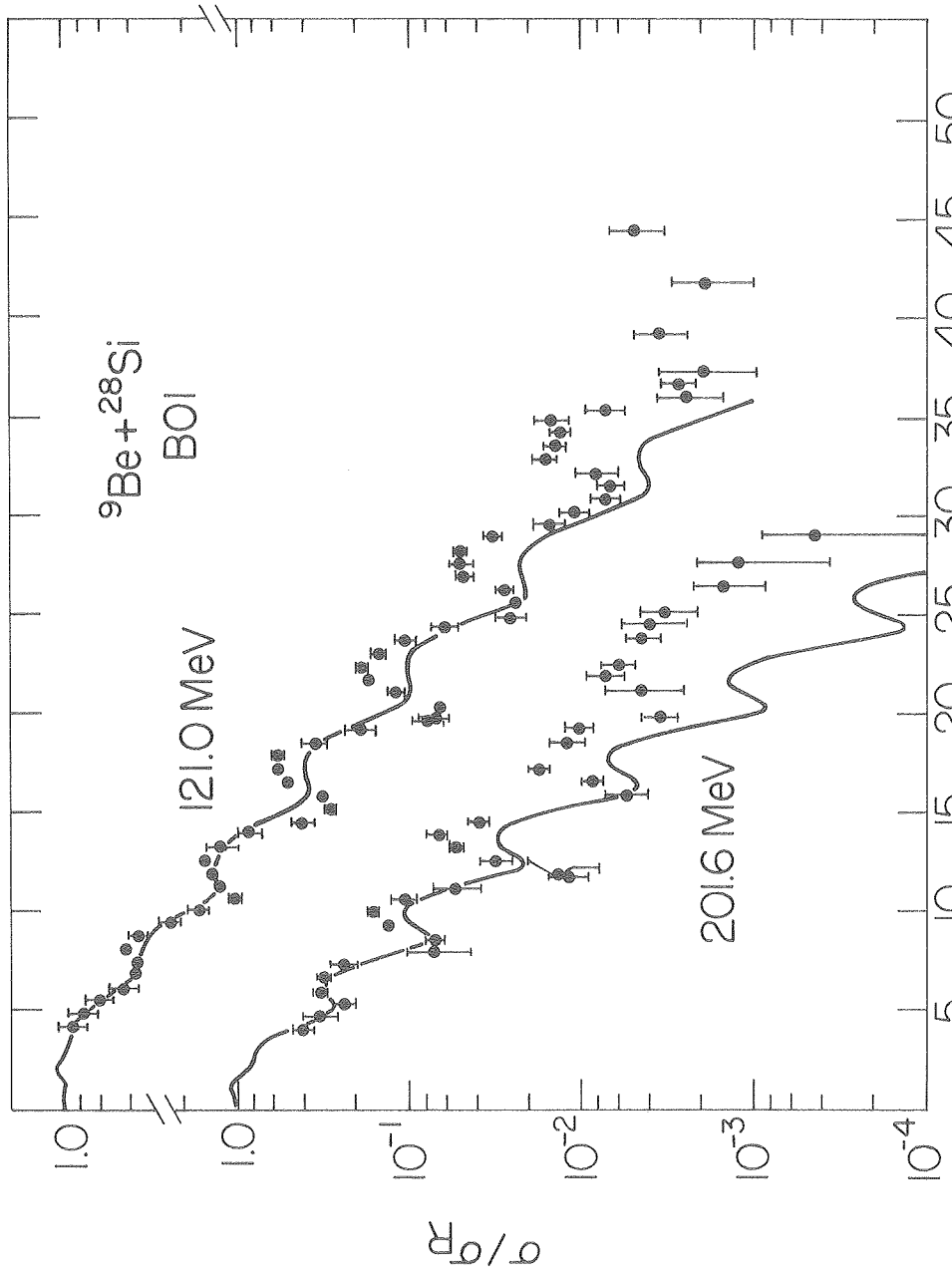

XBL7911-4531

Fig. 5.

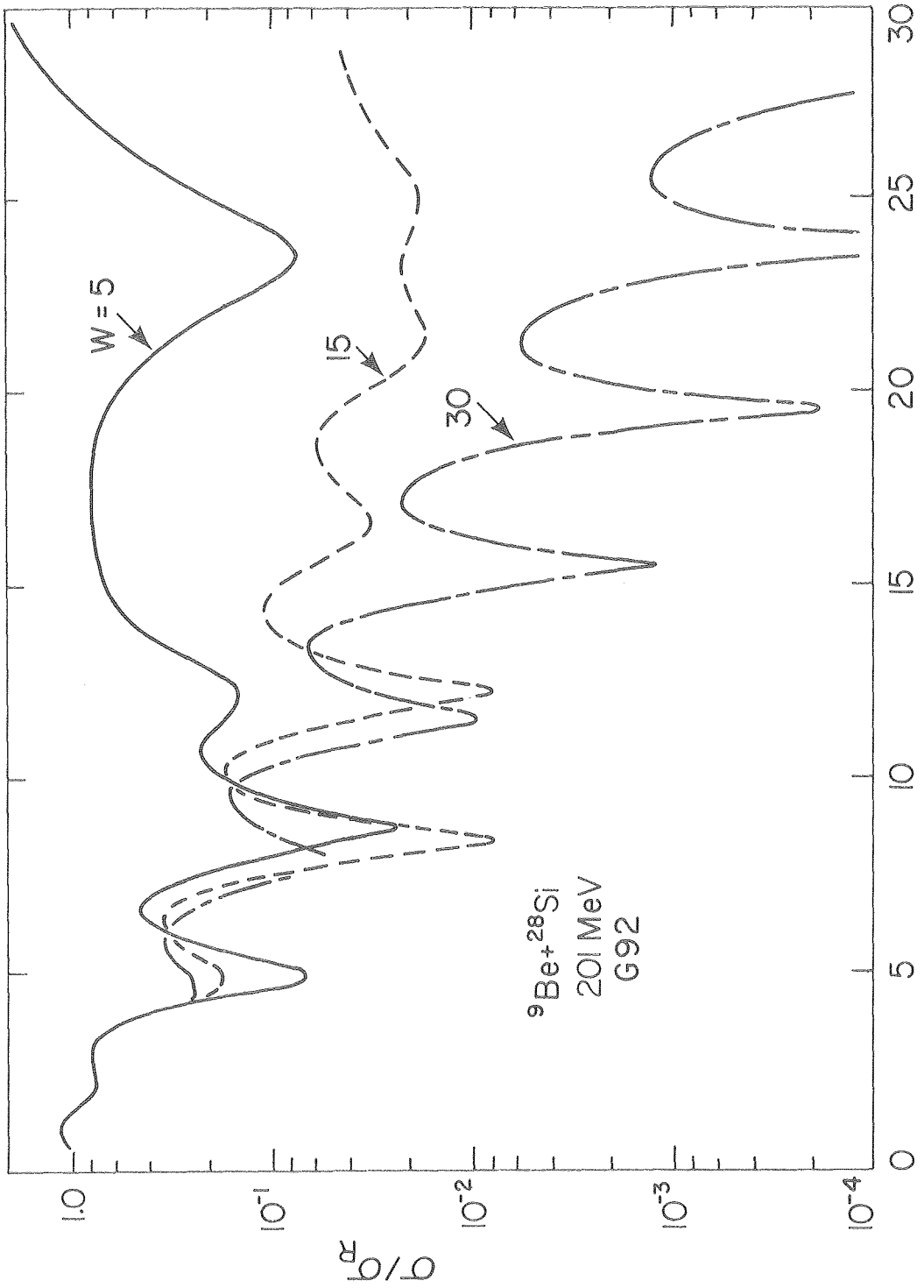

XBL 795 - 1479

Fig. 6.

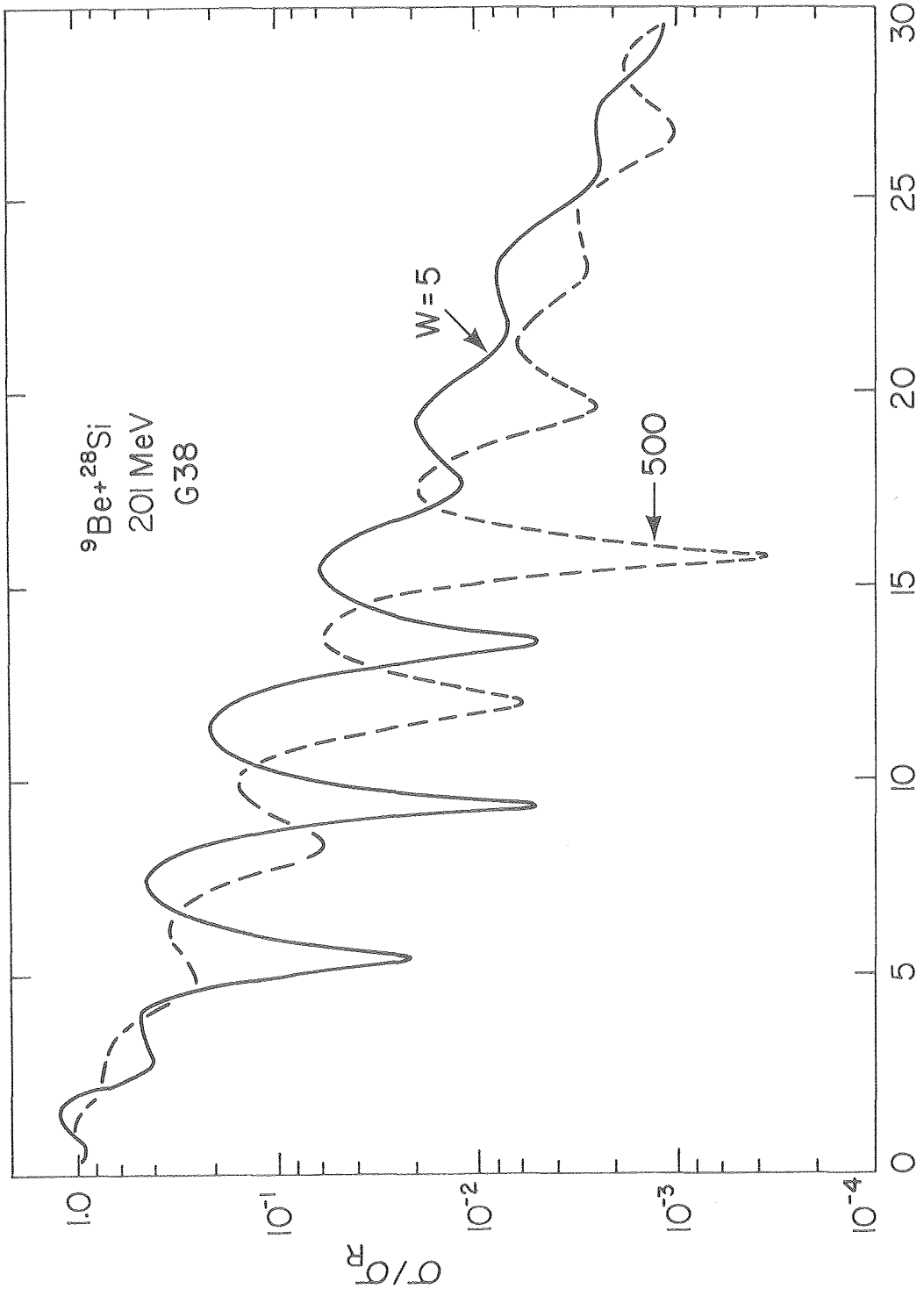

XBL 795 - 1480

Fig. 7.

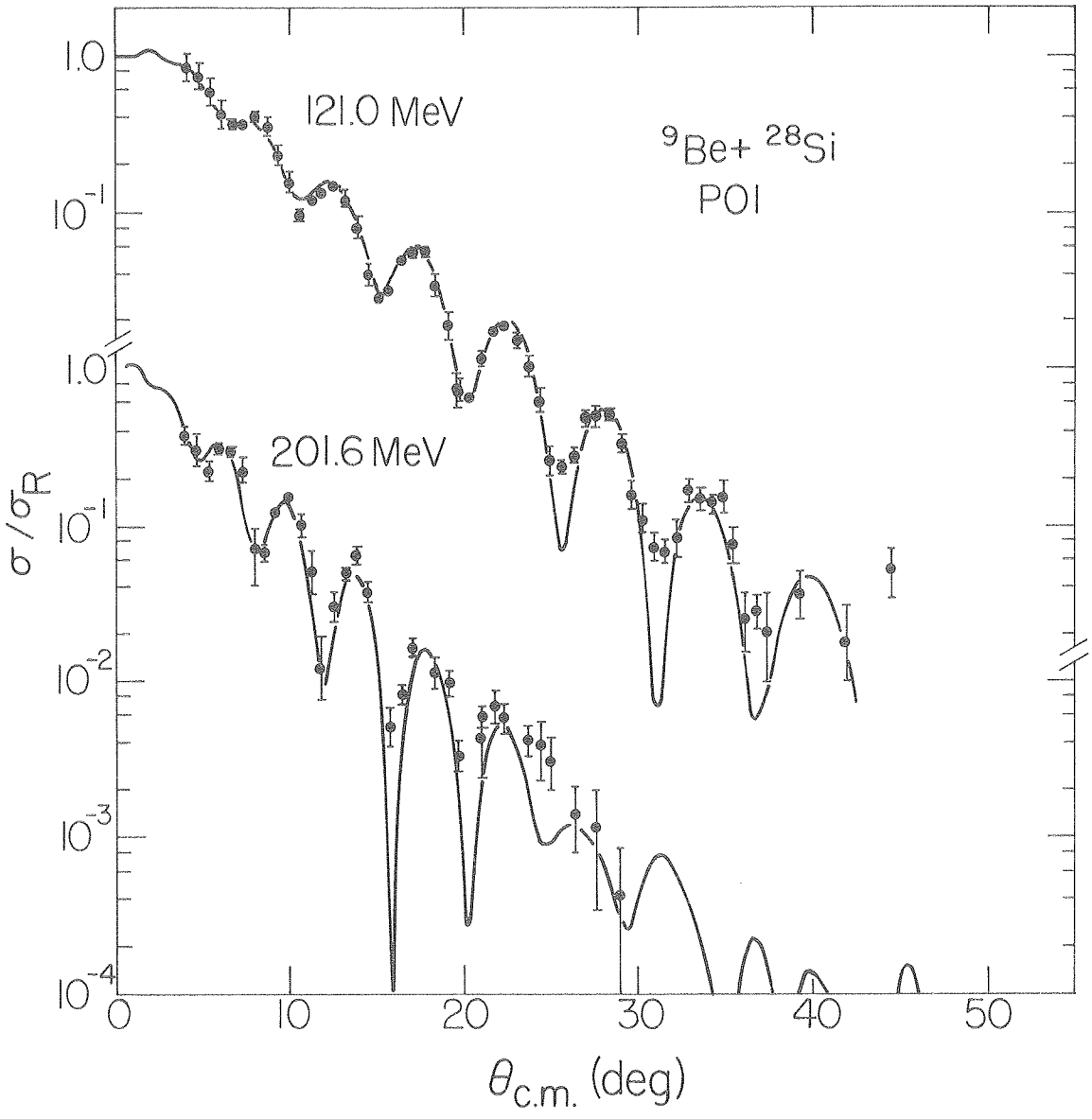

XBL 7911-4536

Fig. 8.

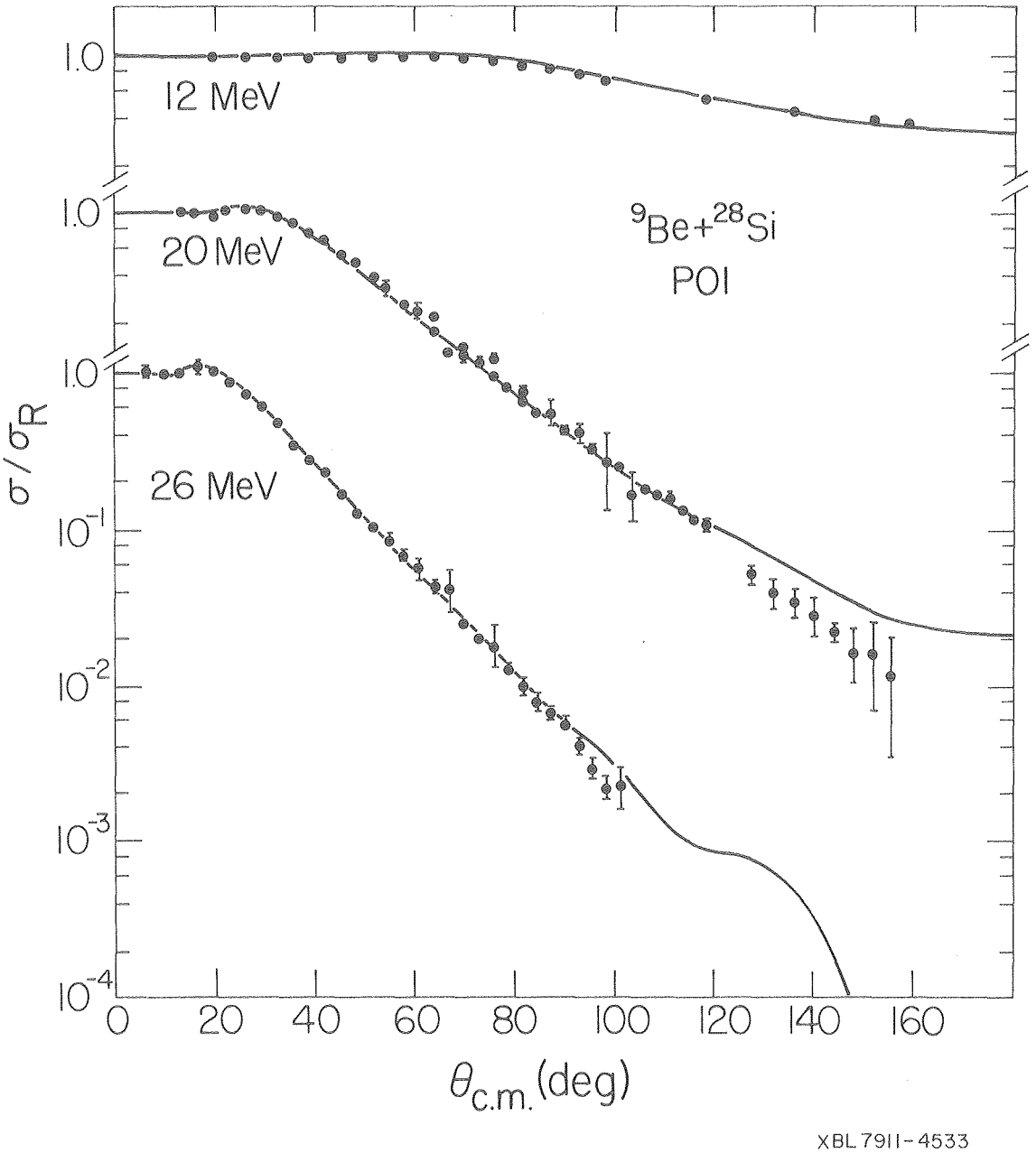
12 MeV
20 MeV
26 MeV
$^{9}Be+^{28}Si$
P01
σ/σ_R
1.0
10^{-1}
10^{-2}
10^{-3}
10^{-4}
0
20
40
60
80
100
120
140
160
$\theta_{c.m.}$ (deg)
XBL 7911-4533

Fig. 9.

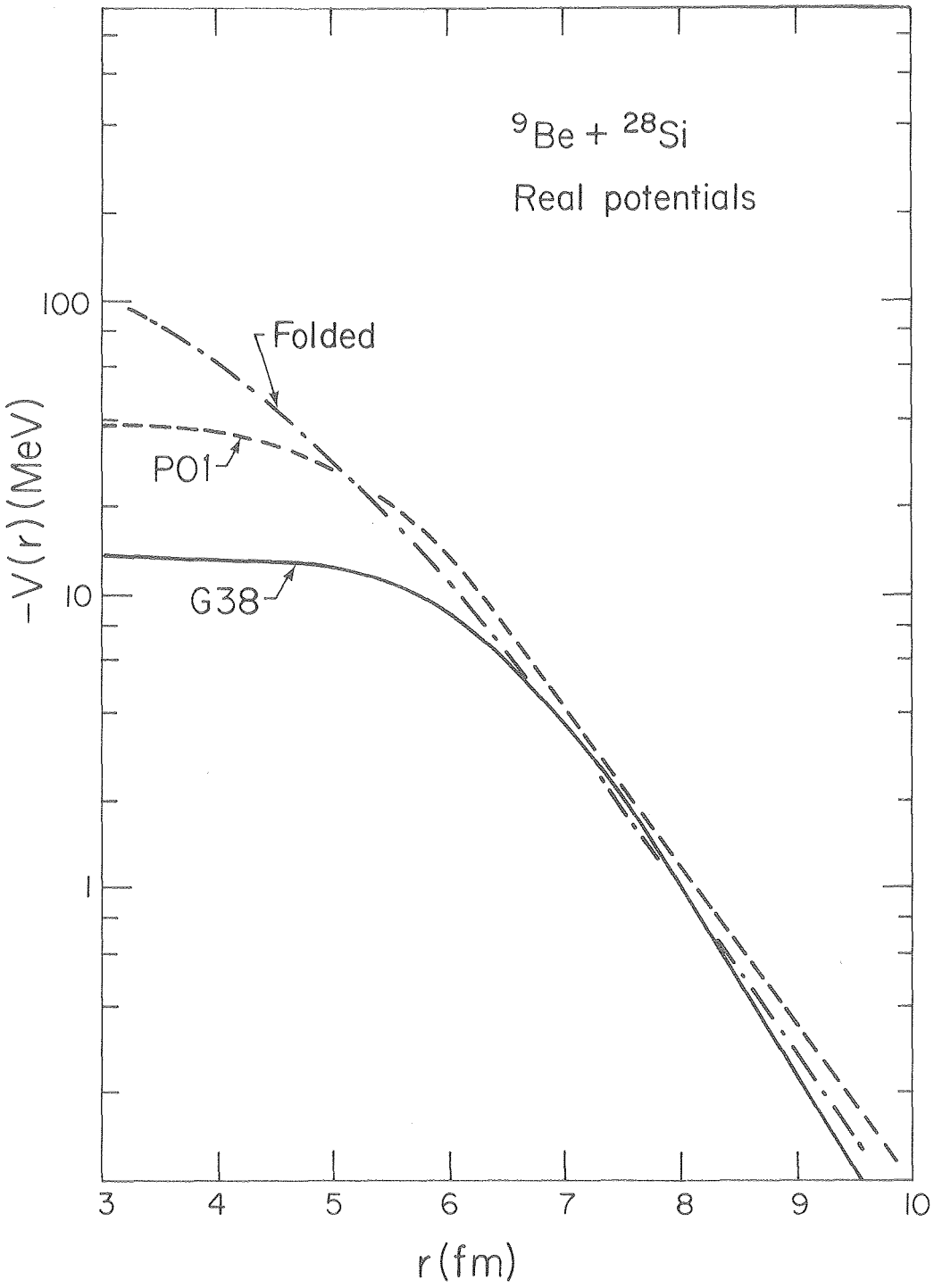

XBL 7910-4527

Fig. 10.

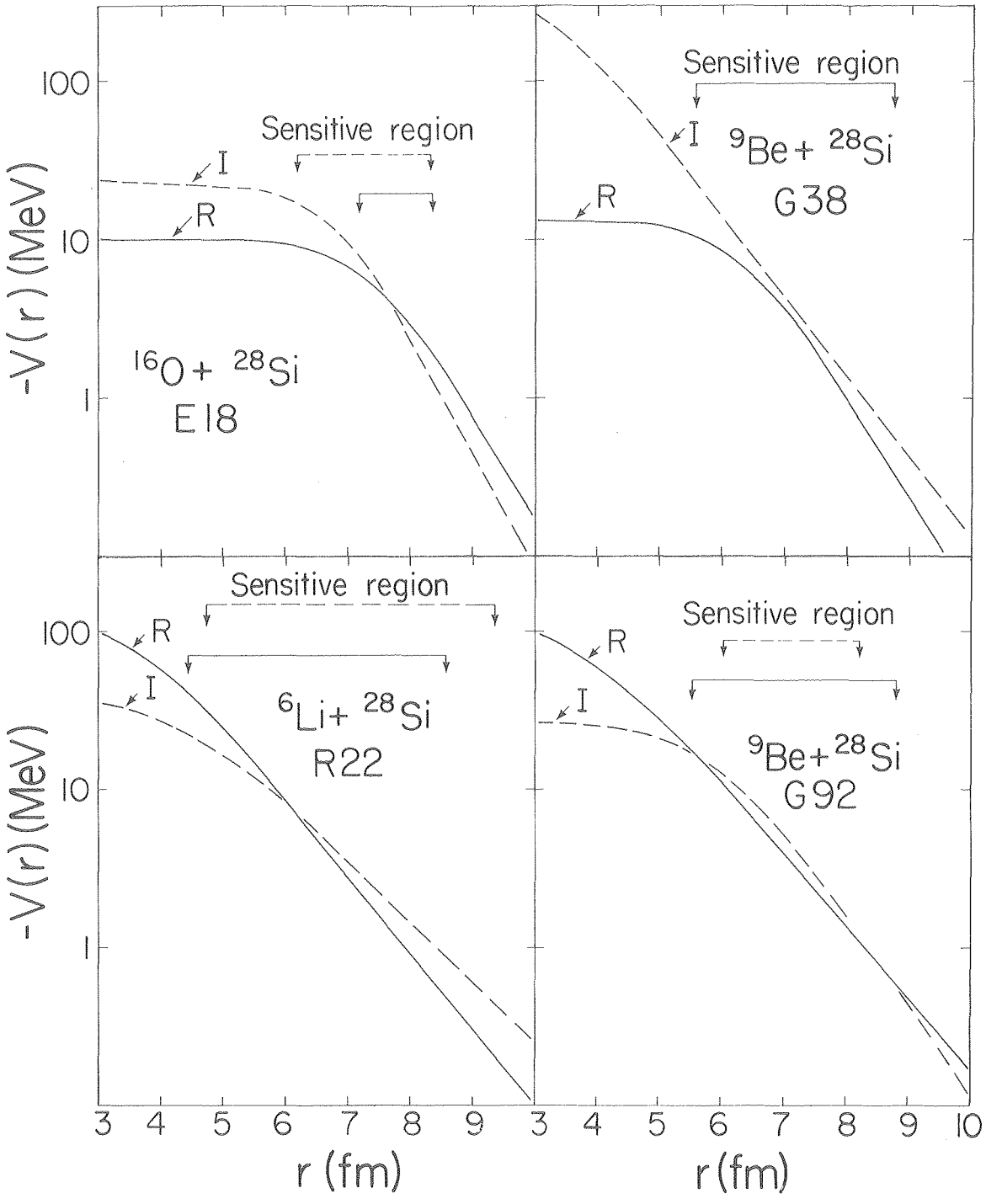

XBL 7910-12378

Fig. 11.

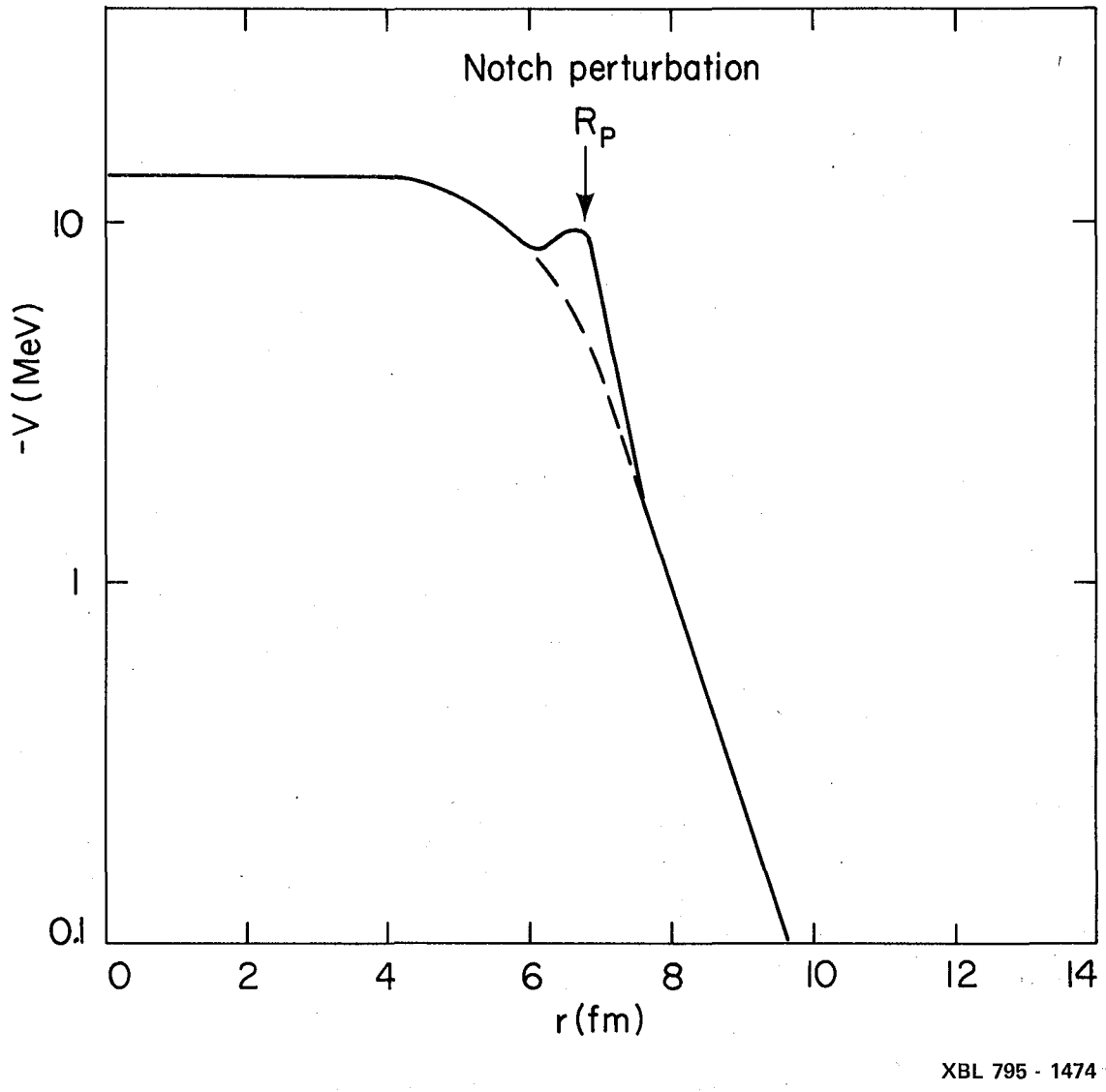
Notch perturbation
R_P
10
1
0.1
-V (MeV)
0
2
4
6
8
10
12
14
r (fm)
XBL 795 - 1474

Fig. 12.

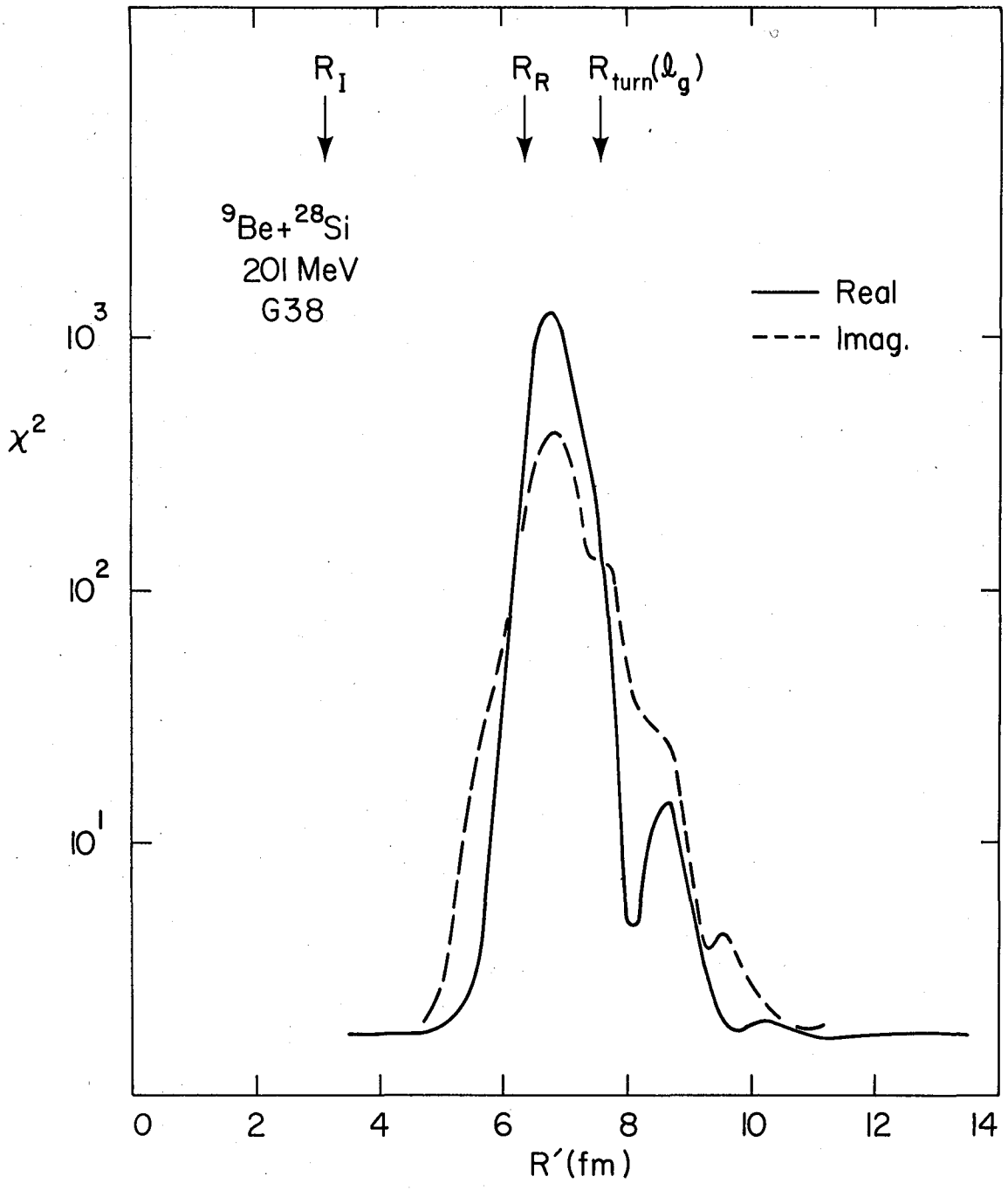
R_I
R_R
$R_{turn}(\ell_g)$
$^9Be+^{28}Si$
201 MeV
G38
Real
Imag.
10^3
10^2
10^1
χ^2
0
2
4
6
8
10
12
14
R′(fm)
XBL 795 - 1473

Fig. 13.

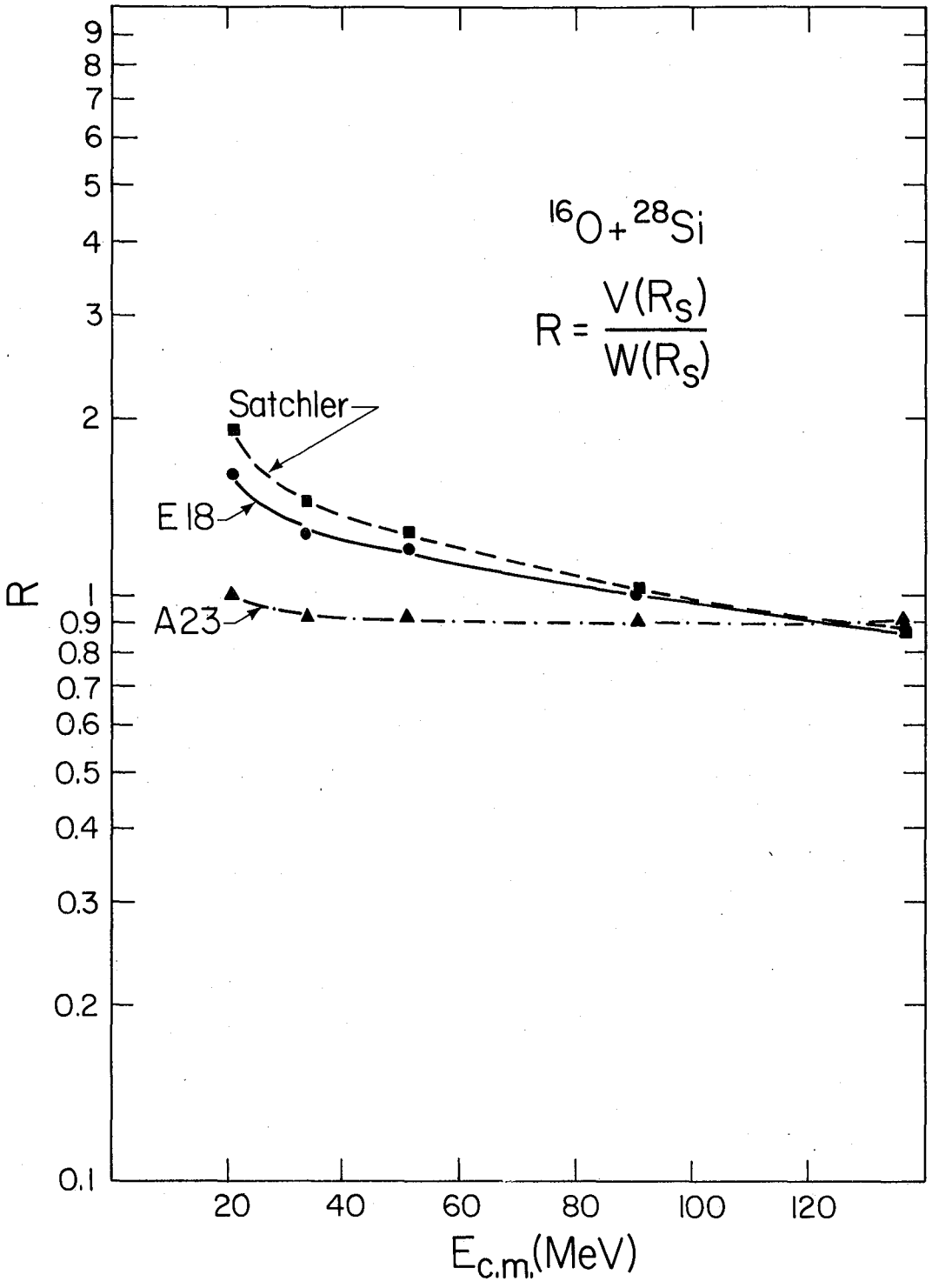

XBL 795-1695

Fig. 14.

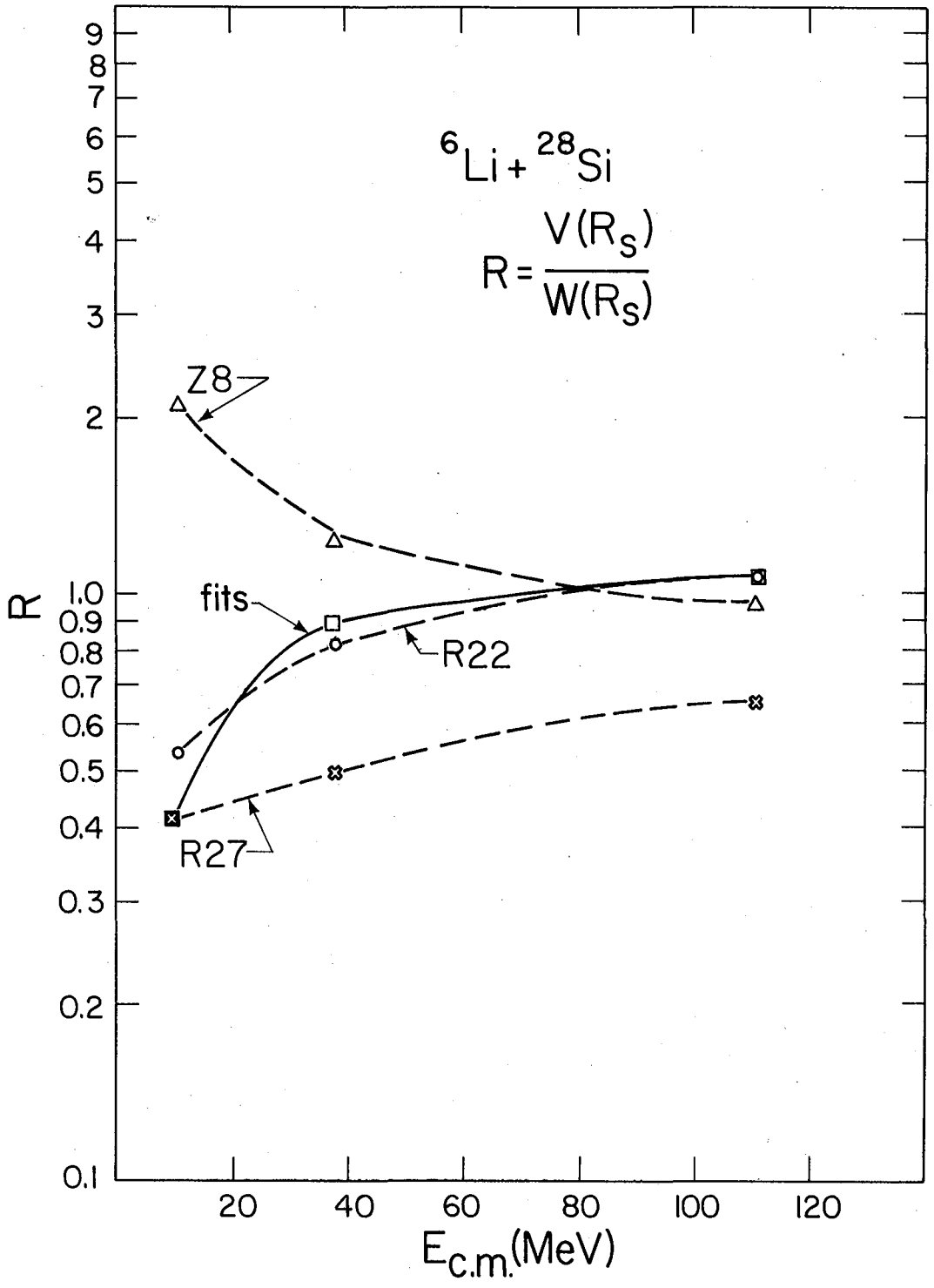

XBL 796-1966

Fig. 15.

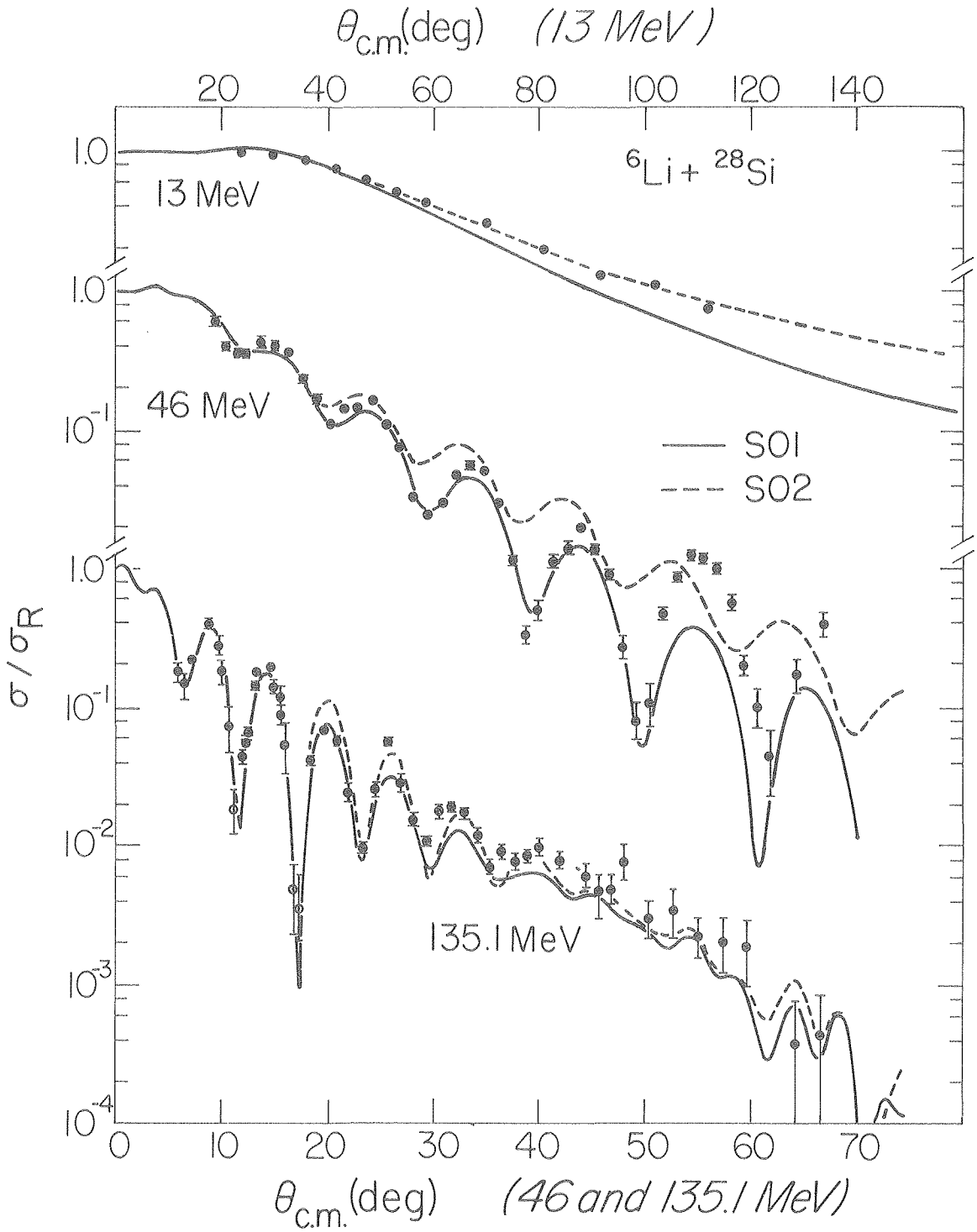

XBL 7911 - 4530

Fig. 16.

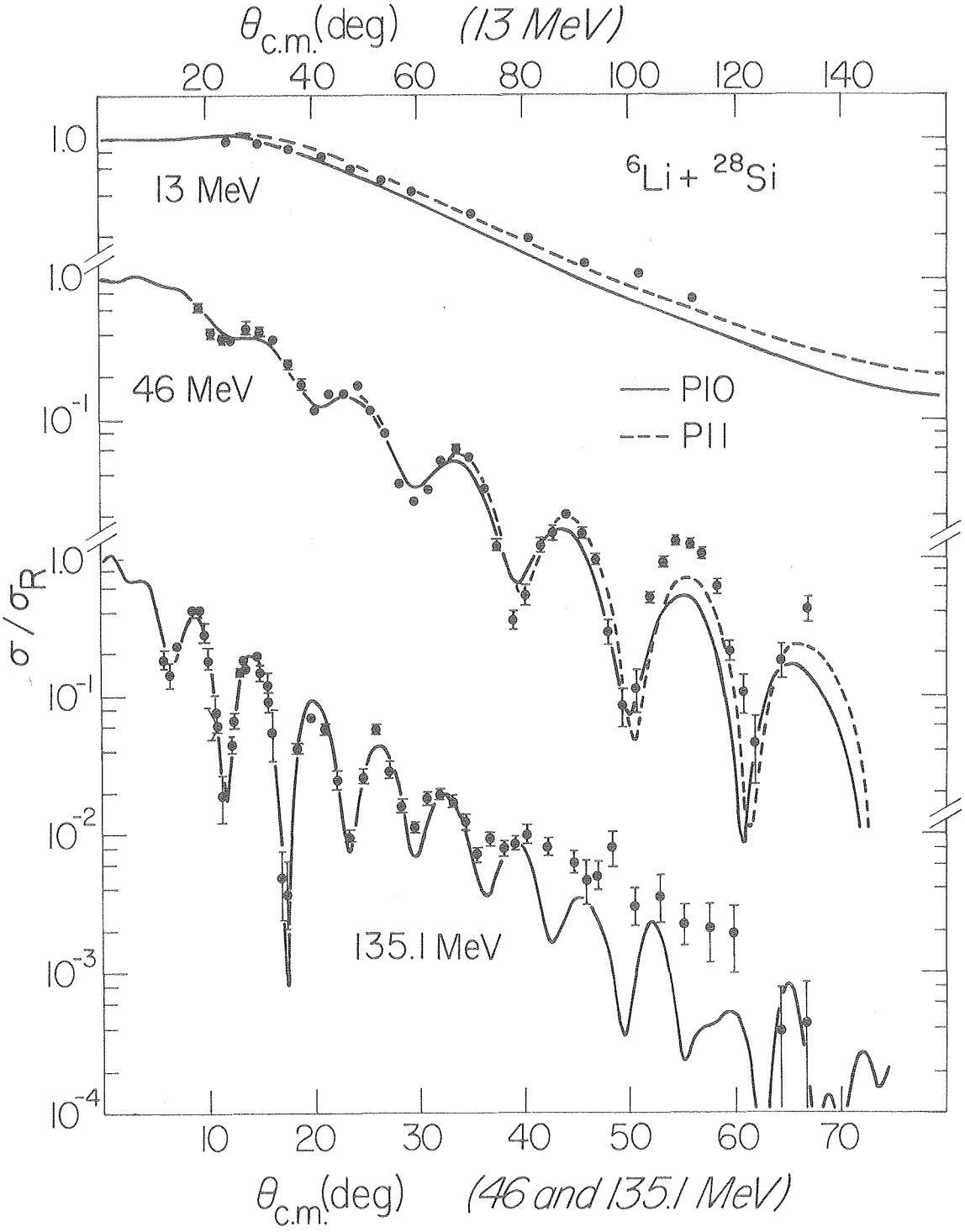

XBL 7910-4529

Fig. 17.

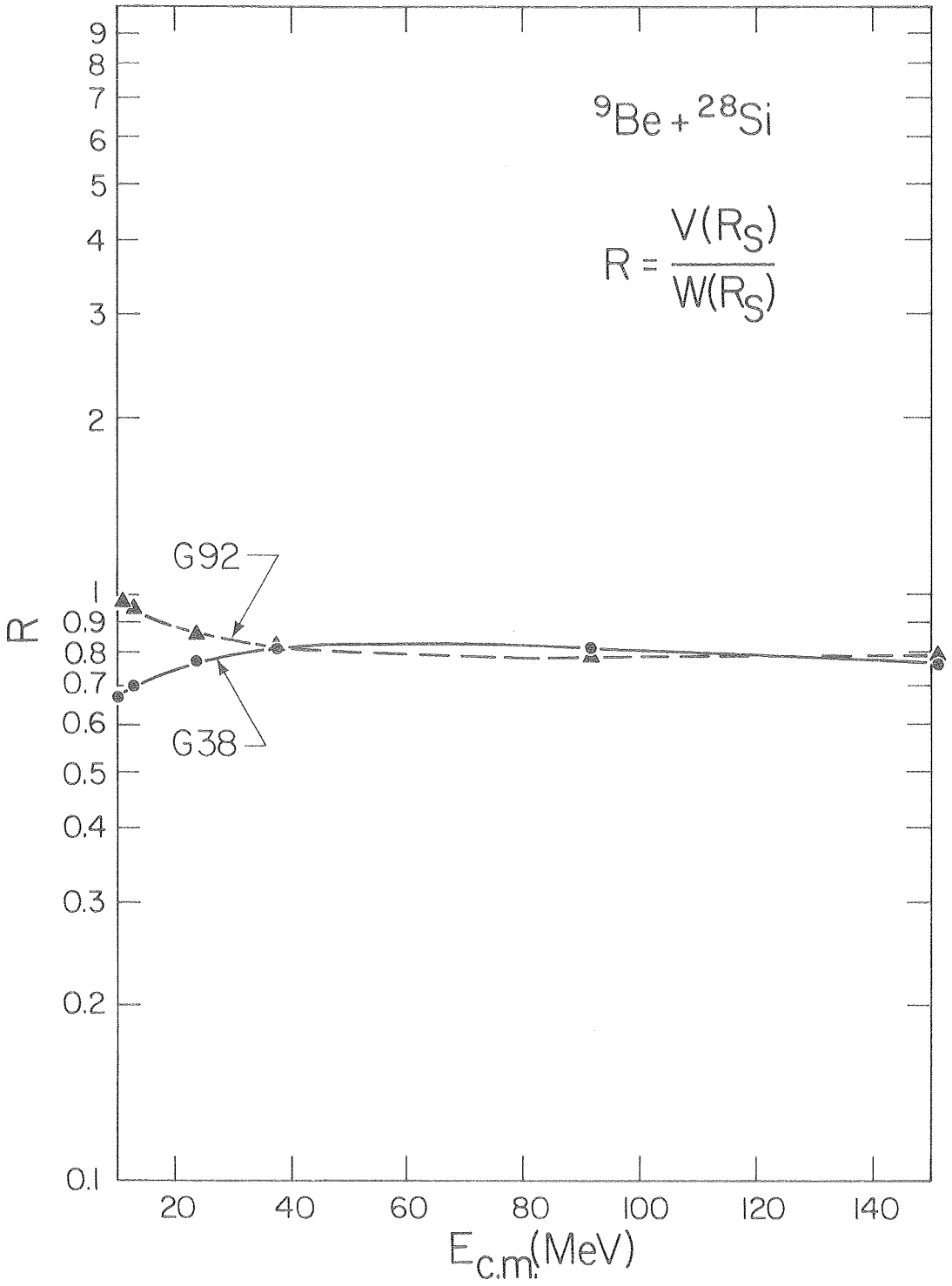

XBL 796-1967

Fig. 18.

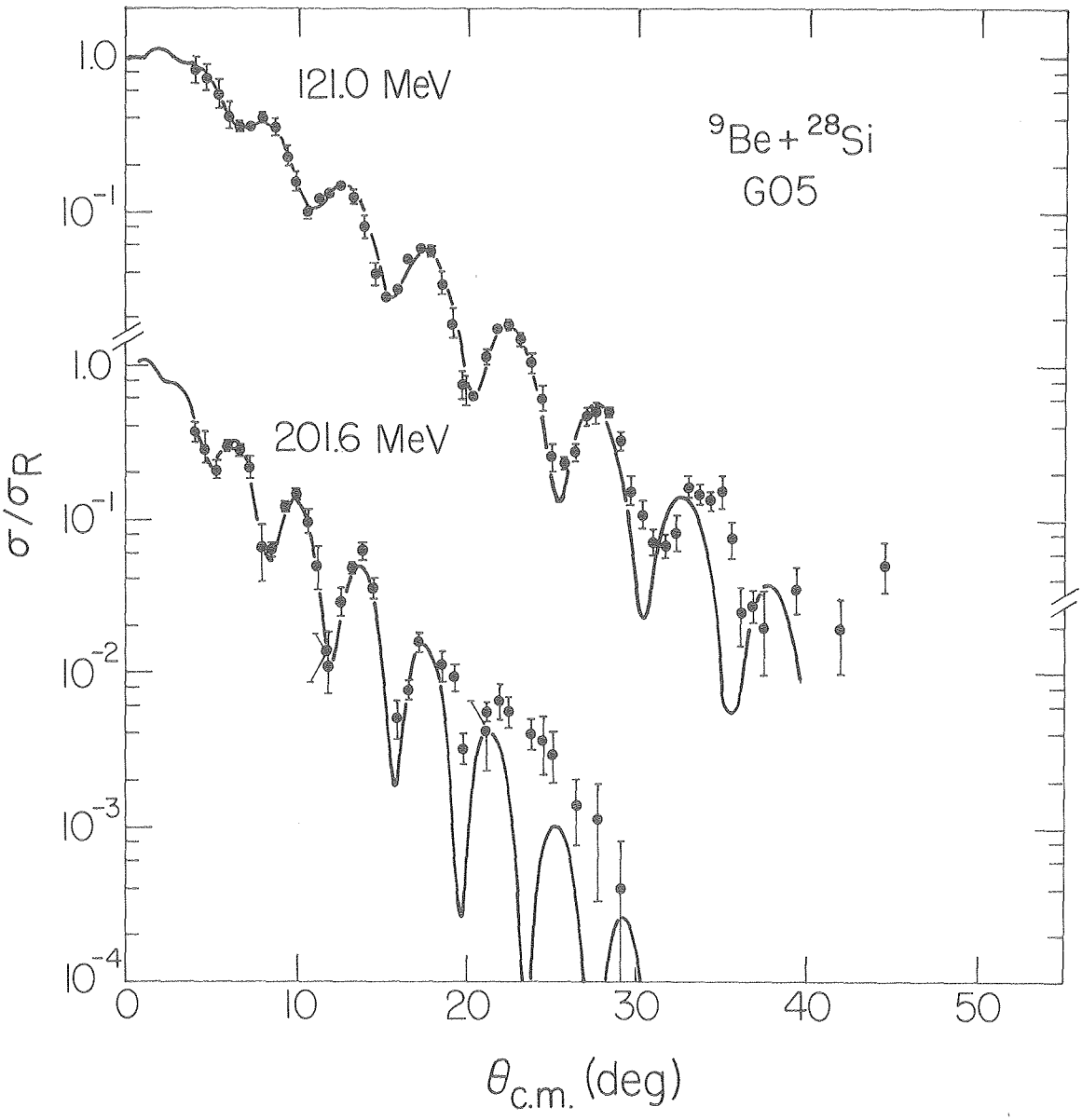

XBL 7911 – 4535

Fig. 19.

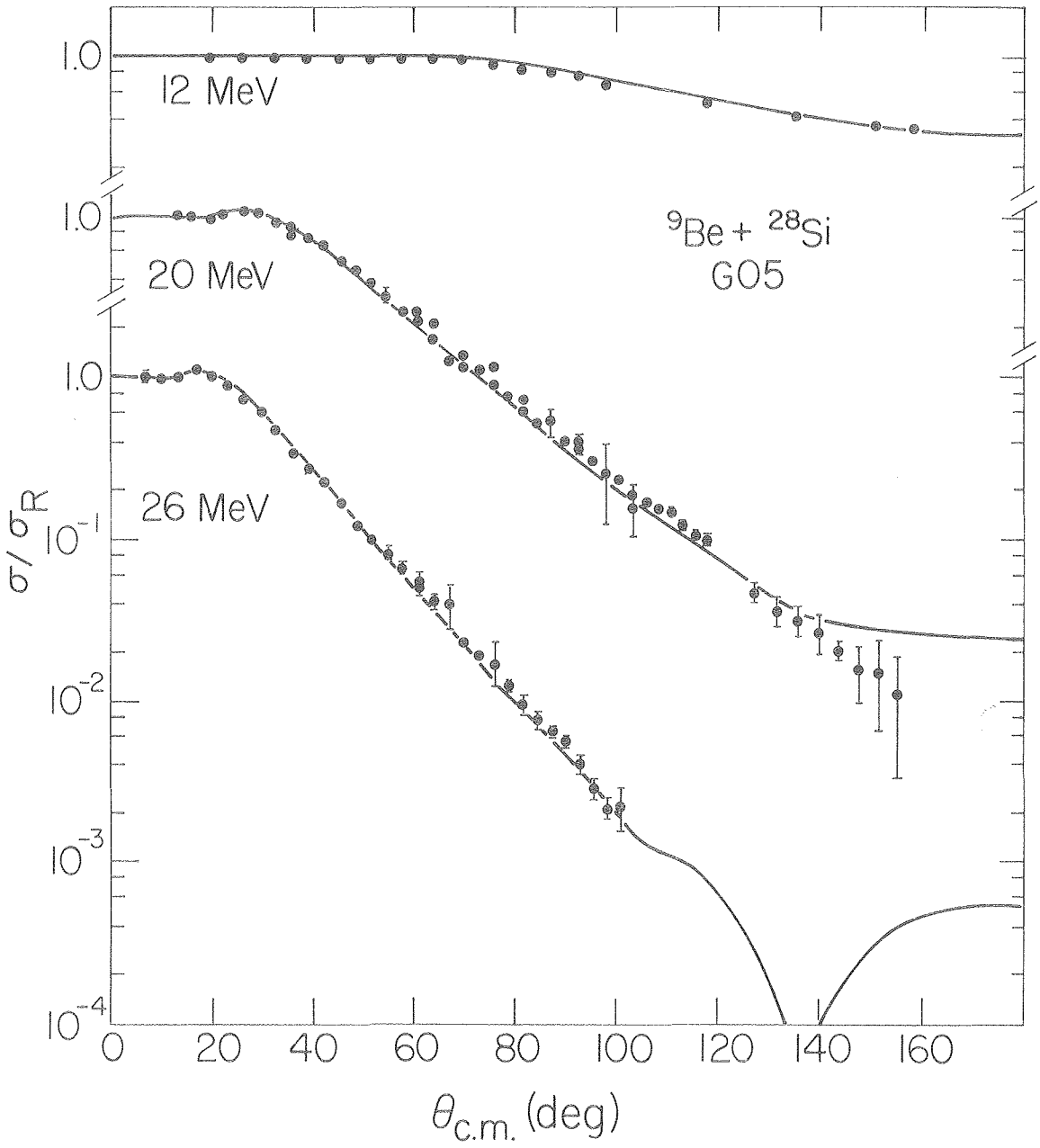

XBL 7911-4534

Fig. 20.

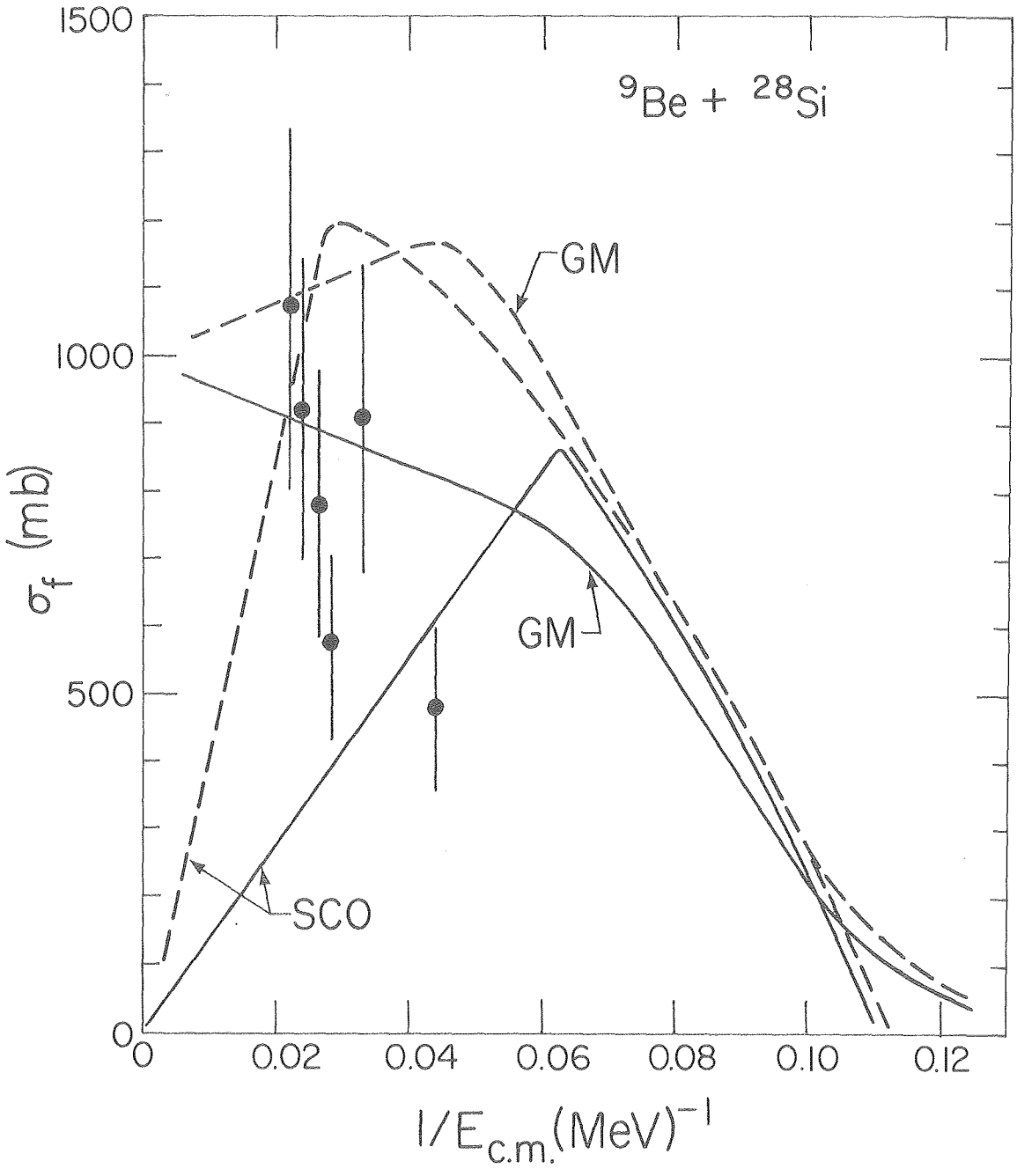

XBL 7910-4528

Fig. 21.